SIMULATION OF THREE-DIMENSIONAL LAMINAR FLOW AND

HEAT TRANSFER IN AN ARRAY OF PARALLEL

MICROCHANNELS

A Thesis

by

JUSTIN DALE MLCAK

Submitted to the Office of Graduate Studies of
Texas A&M University
in partial fulfillment of the requirements for the degree of

MASTER OF SCIENCE

May 2007

Major Subject: Mechanical Engineering

SIMULATION OF THREE-DIMENSIONAL LAMINAR FLOW AND

HEAT TRANSFER IN AN ARRAY OF PARALLEL

MICROCHANNELS

A Thesis

by

JUSTIN DALE MLCAK

Submitted to the Office of Graduate Studies of
Texas A&M University
in partial fulfillment of the requirements for the degree of

MASTER OF SCIENCE

Approved by:

Chair of Committee,   N.K. Anand
Committee Members,   J.C. Han
                        Yassin A. Hassan
                        Michael J. Rightley
Head of Department,   Sai C. Lau

May 2007

Major Subject: Mechanical Engineering

ABSTRACT

Simulation of Three-Dimensional Laminar Flow and Heat Transfer in an Array of

Parallel Microchannels. (May 2007)

Justin Dale Mlcak, B.S., Texas A&M University

Chair of Advisory Committee: Dr. N.K. Anand

Heat transfer and fluid flow are studied numerically for a repeating microchannel array with water as the circulating fluid. Generalized transport equations are discretized and solved in three dimensions for velocities, pressure, and temperature. The SIMPLE algorithm is used to link pressure and velocity fields, and a thermally repeated boundary condition is applied along the repeating direction to model the repeating nature of the geometry. The computational domain includes solid silicon and fluid regions. The fluid region consists of a microchannel with a hydraulic diameter of 85.58μm. Independent parameters that were varied in this study are channel aspect ratio and Reynolds number. The aspect ratios range from 0.10 to 1.0 and Reynolds number ranges from 50 to 400. A constant heat flux of 90 W/cm^2 is applied to the northern face of the computational domain, which simulates thermal energy generation from an integrated circuit.

A simplified model is validated against analytical fully developed flow results and a grid independence study is performed for the complete model. The numerical results for apparent friction coefficient and convective thermal resistance at the channel inlet and exit for the 0.317 aspect ratio are compared with the experimental data. The numerical results closely match the experimental data. This close matching lends

credibility to this method for predicting flows and temperatures of water and the silicon substrate in microchannels.

Apparent friction coefficients linearly increase with Reynolds number, which is explained by increased entry length for higher Reynolds number flows. The mean temperature of water in the microchannels also linearly increases with channel length after a short thermal entry region. Inlet and outlet thermal resistance values monotonically decrease with increasing Reynolds number and increase with increasing aspect ratio.

Thermal and friction coefficient results for large aspect ratios (1 and 0.75) do not differ significantly, but results for small aspect ratios (0.1 and 0.25) notably differ from results of other aspect ratios.

To a true engineer, my late paternal grandfather *Henry R. Mlcak.* A man of patience,

faith, honesty, science, and family.

ACKNOWLEDGMENTS

I would like to thank many people for their support, guidance, and patience throughout my graduate studies. First and foremost, I thank my committee chair, Dr. N.K. Anand for his excellent teaching and guidance in my coursework and research. His substantial knowledge in the areas of numerical methods and the thermal fluid sciences is impressive. He is also an admirable role model and leader within the university, and I am eternally thankful for his patience with me during my graduate studies. I am also thankful to him for his help in obtaining funding for me throughout my studies.

This thesis would not be complete without approval and suggestions from members of my thesis committee. I am thankful to Dr. J.C. Han, Dr. Yassin Hassan, and Dr. Mike Rightley for their willingness to serve on my committee and for taking time to approve and comment on my work. I am especially thankful to Dr. Rightley of Sandia National Laboratories for his willingness to serve on my committee even when it was not required, and I am grateful for the leadership and technical skills I have learned while a member of his team.

Additionally, I would like to thank Mike Sjulin and Robert Koss of Sandia National Laboratories for funding my research work and for providing me with a research computer. I am grateful for the many good times and thought provoking conversations with the many intelligent people at Sandia National Laboratories.

Furthermore, I would like to thank the Office of Graduate Studies at Texas A&M for awarding me with the Graduate Merit Fellowship as I began my masters. This funding removed a large burden from me during my graduate education. Their patience

with my questions and willingness to work with me while I was away from campus are greatly appreciated.

I would like to also acknowledge my co-workers, Minseok Ko, Muhammad Ijaz, Steve Pate, and Tracy Fullerton, for their advice, useful ideas, great conversation, and good times.

On the departmental level, I am thankful to Ms. Kim Moses, Ms. Missy Cornett, and Dr. Sai Lau for their patience and willingness to answer my questions about the graduate degree process and for their willingness to help me set achievable career goals.

Finally, I would like to thank my parents, my sister and brother-in-law, my grandparents and my extended family and friends for their unending love and support during my graduate studies.

TABLE OF CONTENTS

LIST OF TABLES

LIST OF FIGURES

NOMENCLATURE

a	discretization coefficient
A	area of control volume face, m^2
A_c	channel cross-sectional area, m^2
A_t	computational boundary area at y = W, m^2
$A(|P|)$	dimensionless coefficient, represents convection-diffusion at boundary
C	distance between the bottom of the substrate and the channel central axis, m
C^*	friction coefficient
c_p	specific heat at constant pressure, J/(kg K)
D	diffusive conductance
D_h	hydraulic diameter, m
F	convection strength, kg/s
f	friction factor
h	channel height, m
H	computational domain height (y-direction), m
J	total flux
k	thermal conductivity, W/(m K)
K_i	constant term in matrix of discretized equations
Kn	Knudsen number
L	channel length, m
$\dot{m}$	mass flow rate, kg/s
P	Peclet number

p	pressure, Pa
PCV	pressure control volume
Po	Poiseuille number (fRe)
P_s	channel perimeter, m
q''	heat flux, W/m^2
R	residual
Re	Reynolds number
R_t	thermal resistance
S	surface along channel perimeter
S_C	constant source term
S_P	proportional source term
S_T	temperature source term
T	temperature, K
T_m	mean (bulk) temperature, K
T_w	average wall temperature, K
u	x-direction velocity component, m/s
UCV	u-velocity control volume
$\vec{V}$	velocity vector
v	y-direction velocity component, m/s
VCV	v-velocity control volume
W	computational domain width (z-direction), m
w	z-direction velocity component, m/s

w_c	channel width, m
WCV	w-velocity control volume
x	x coordinate direction
y	y coordinate direction
z	z coordinate direction

Greek

α	channel aspect ratio (w/h)
Γ	diffusion coefficient
δ	diffusion length, m
Δ	length of control volume side, m
ε	convergence value
μ	viscosity, N s/m^2
ρ	density, kg/m^3
ϕ	general transport variable

Subscripts

app	apparent
b	bottom (referring to area between nodes)
B	bottom neighbor node
e	east (referring to area between nodes)
f	fluid
E	eastern neighbor node
n	north (referring to area between nodes)

N	northern neighbor node
nb	all neighboring nodes
P	central point
s	south (referring to area between nodes)
S	southern neighbor node
t	top (referring to area between nodes)
T	top neighbor node
w	west (referring to area between nodes)
W	western neighbor node

Superscripts

'	pressure correction
*	guessed value
T	referring to temperature
u	referring to x-direction velocity
v	referring to y-direction velocity
w	referring to z-direction velocity

1. INTRODUCTION

Over two and a half decades ago, microchannels emerged as a potential solution for dissipating thermal energy from densely packed integrated circuitry. Proposals and research indicated that high heat fluxes could be dissipated by a fluid passing through microchannels that offer an increased surface area to volume ratio. Though dimensions are not formally defined, microchannels are typically rectangular channels with hydraulic diameter between 1μm and 200μm. Heat fluxes from integrated circuits have exceeded $100W/cm^2$ [1], and in the early 1980's, Tuckerman and Pease [2] reported heat flux dissipation as high as $790W/cm^2$ for a microchannel heat sink with a 71ºC mean fluid temperature rise. As the density of integrated circuits increases and the heat flux multiplies, there is an increasing need for more research into microchannel design, performance, and application.

Microchannels can be formed directly on the chip (integrated circuit) substrate. The advantage of the location on the substrate is the reduced thermal resistance from heat source to heat sink [2]. To avoid any disruption of circuit function, the microchannels can be built onto or etched into the electrically inactive side of the chip. The work of early microchannel pioneers initiated research and development of other micro-fluidic devices including ink jet printers, fuel cells, micropumps, heat exchangers, chemical reactors, and biomedical devices.

This thesis follows the style of *Numerical Heat Transfer*.

This research work includes modeling fluid flow and heat transfer for water flowing in an array of parallel rectangular microchannels with an 86.58μm hydraulic diameter as shown in Figure 1.1. This research models the case studied experimentally by Kawano et al. [3]. In addition, five different aspect ratios are considered in this work. The experiments use a heat source to model constant heat flux coming from an integrated circuit.

The microchannel array has a sump at both the inlet and the outlet of the channels for the purpose of ensuring uniformity of velocity distributions and pressure drops for the fluid in each of the channels. With a sump, flow maldistributions may occur in channels along the edge of the array, which may be caused by uneven pressure drop and uneven heat flux. The channels are repeated in the transverse (z) direction, and Figure 1.2 shows one slice of the repeating geometry including one channel and surrounding solid region that will be modeled. This approach greatly simplifies the computational procedure and is valid for most channels except those along the outer edges. The sump may ensure a uniform pressure at each channel inlet, but temperature maldistributions may cause local fluid viscosity variations. Changes in the local fluid viscosity can change velocity profiles and friction factor and result in flow maldistributions among the channels.

1.1 Motivation

As the presence of microchannels on integrated circuitry substrates will likely be a necessary feature of densely packed electronics, much research work will be devoted to the simulation, design, and optimization of such devices. While some microchannel
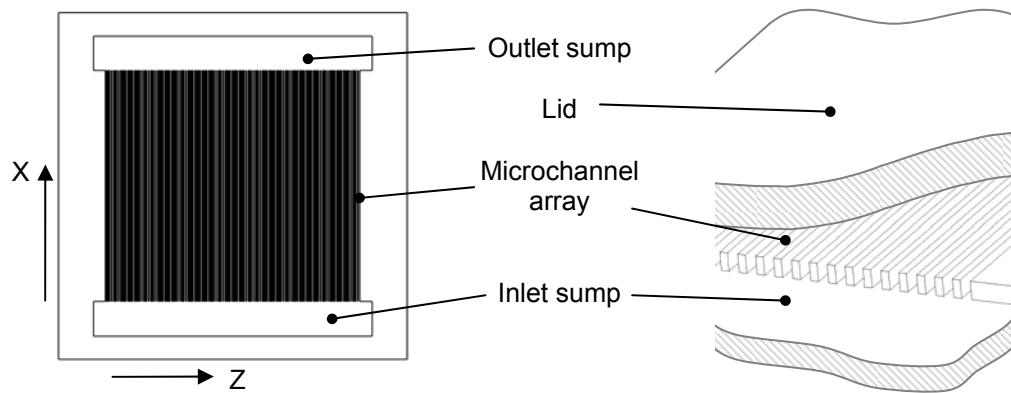
Figure 1.1. Top view and 3-D cut away of microchannel array.
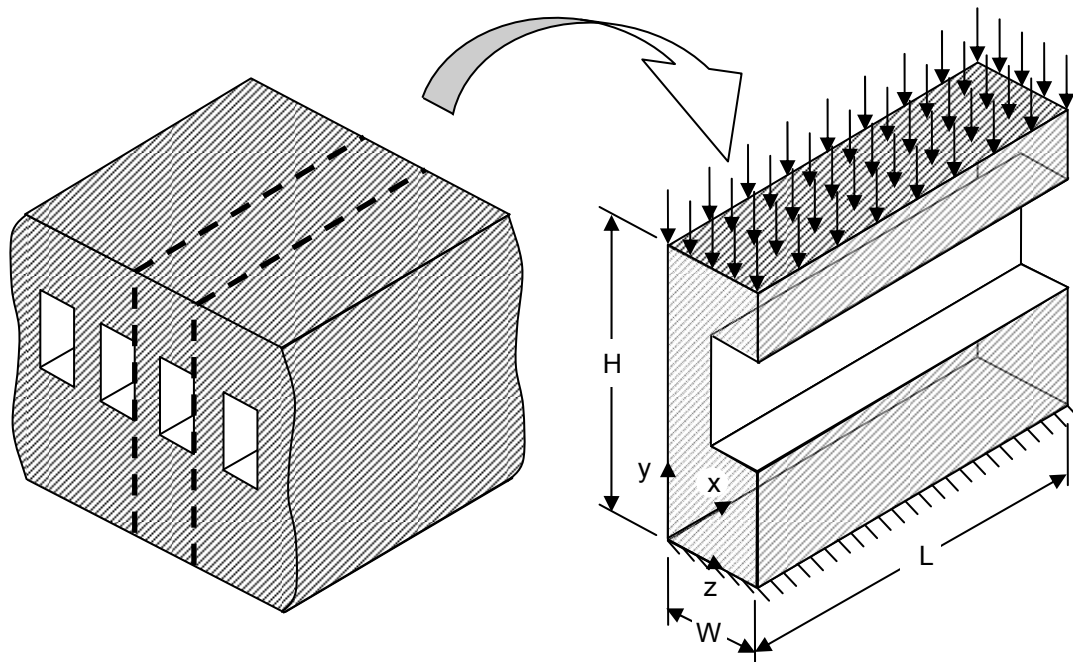
Figure 1.2. Repeating microchannel geometry and single computational domain used for simulating entire array.

devices are well understood, many researchers do not have a fundamental understanding of the thermal and hydraulic performance of microchannel devices. With unknown thermohydraulic performance of fluids within microchannels, these devices may not be designed for optimum heat transfer or pressure drop. Not only does this affect the design of the microchannel device, but this also impacts the design of external pumping and thermal management systems.

Existing experimental data and analytical models for heat transfer and fluid flow sometimes differ greatly from one another. While some experimenters claim conventional theory is not applicable to microchannel flow, others indicate that conventional theory is an accurate predictor of microflows [4]. Furthermore, experiments performed by different investigators often give conflicting results [4], which contributes to confusion within this field of research. Over the past two decades, over a dozen experimental and physical conditions have been suspected as factors that effect fluid flow and heat transfer in microchannels [5], and combining each factor into a working simulation of microchannel flow and heat transfer would be a difficult task. Clearly, widely-accepted theories are needed that explain the behavior of fluid flow and heat transfer on the micro-level.

This research work aims at a better understanding of thermal and hydraulic performance of water in a parallel series of rectangular microchannels. A finite volume technique [6] is used to solve the three-dimensional flow and energy equations in both the solid and the liquid regions.

1.2   Objectives

The research objectives in the present study are:

1. To develop a numerical code that can be used to simulate three-dimensional velocity distributions, pressure distributions, and temperature distributions in a parallel array of rectangular microchannels.

2. To numerically implement the thermally repeated boundary condition for the repeating series of microchannels.

3. To compare the apparent friction coefficient and thermal resistance obtained from the numerical simulation to available experimental data [3].

4. To present results of the numerical simulation in the form of friction coefficient required pumping pressure vs. flowrate, thermal resistance, and maximum substrate temperature for Reynolds number ranging from 50 to 400 and aspect ratio ranging from 0.1 to 1.0.

5. To numerically analyze the effect of viscous dissipation on the bulk temperature for one case of aspect ratio.

1.3   Thesis Outline

This thesis is a documentation of the creation, implementation, and results of a numerical study that solves for velocity, pressure, and temperature in a three dimensional microchannel array.

In Section 1, an introduction to the problem is coupled with an explanation of microchannel terminology. Several statements about the need for microchannel research

are given which act as the impetus for this work, and direct statements define the objectives of this work.

In Section 2, a review of the open literature pertaining to the topic of heat transfer and fluid flow in microchannels is presented, which includes work of both experimental and numerical investigators.

The geometries that are to be considered in this study are presented in Section 3, and this is followed by the relevant mathematical equations and boundary conditions that describe fluid flow and heat transfer. Since an objective of this work is to compare the numerical results with experimental data, Section 3 also includes a brief description of the experimental conditions that produced the experimental data.

The numerical procedure, including discretization method, grid generation, and solution algorithm, are included in Section 4. While the numerical code is not provided in this section, the methods by which it was produced are included.

Section 5 contains information about the validation and grid independence studies that were performed which give credibility to the numerical code. The code is validated by viewing numerical symmetry, comparing fully-developed flow values to analytical results, and performing an overall energy balance. The comparison of the numerical results to experimental data is not considered in Section 5 because no set of experiments has been widely accepted as a baseline case for validation purposes.

Results of the numerical code are presented and discussed in Section 6. The results include friction coefficient, system characteristic, thermal resistance, and maximum substrate temperature for Reynolds number ranging from 50 to 400 and

channel aspect ratio ranging from 0.10 to 1.0. Also, the numerical results are compared to experimental results for the case of a 0.317 aspect ratio.

Lastly, Section 7 includes a summary and conclusions obtained from the numerical work and results, and suggestions for future work in the area of modeling fluid flow and heat transfer in microchannels are discussed.

2. PRIOR WORK

Many investigators cite differences between micro-scale and macro-scale fluid flow and heat transfer, while various other investigators cite similarities between the flow regimes. Beginning the study, it is necessary to understand the scale on which the flow and thermal physics occur. Among other researchers, Bontemps [5] explains the usefulness of the Knudsen number (Kn) as a validity indicator of the continuum hypothesis for a fluid in a channel of a specified length scale. The Knudsen number is the ratio of the molecular mean free path and the channel characteristic length, and a very small value of Kn will mean that the channel is significantly larger than the distance between fluid molecules. In this case, the fluid can be treated as a continuum, and Navier Stokes equations and standard no-slip boundary conditions apply.

Further research has indicated that for increasing Kn, standard boundary conditions (zero fluid velocity at boundary) do not apply, and for even larger Kn, molecular flow effects must be considered because the fluid can no longer be treated as a continuum. The mean molecular free path is approximately 8nm for liquid water, and the characteristic length of the microchannels for the proposed work is 21.7μm, which makes Kn=3.70×10^{-4}. Figure 2.1 illustrates appropriate fluid flow models with respect to Knudsen number [5]. As shown by the point of interest for liquid water in the figure, the Navier Stokes equations and standard boundary conditions apply to the proposed work. While the Knudsen number indicates that Navier Stokes equations and no-slip boundary conditions are applicable for liquid microflows with this length scale, the same is not true for gas microflows. The average mean molecular free path for air is

approximately 70nm, which makes Kn=3.24×10^{-3}, a value that is clearly in the range of slip boundary conditions.
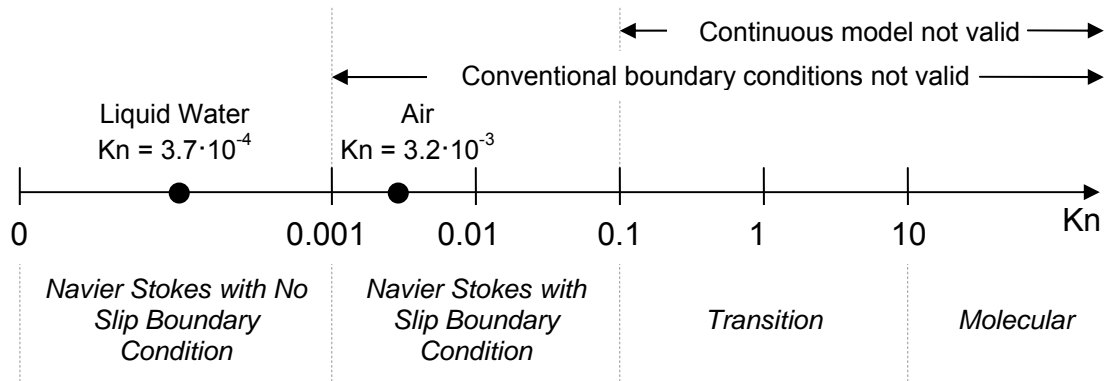
Figure 2.1.   Assumed fluid flow model as a function of Knudsen number (Kn) (adapted from [5]).

Nearly all sources of experimental data for laminar microchannel flows make some attempt to compare data against the Navier Stokes and energy equations, and some investigators try to propose new theories to explain observed phenomena. Often times, the assumptions of hydrodynamic and thermally fully developed flow are used, which can greatly simplify the non-linear equations, but this assumption is not always correct. Currently, there appears to be no widely accepted method for modeling thermohydraulic performance within microchannels.

Figure 2.2 shows a comparison of friction factor data for several different microchannel flow experiments that was compiled by Papautsky et al. [7], and the data are evenly scattered above and below the value predicted by the fully-developed flow reduction from the Navier Stokes equations. References given in Figure 2.2 are the results of Papautsky et al. [7] that the present author could review and validate, while

Papautsky et al. [7] provides a complete set of references. Similar results are reported for Nusselt number.
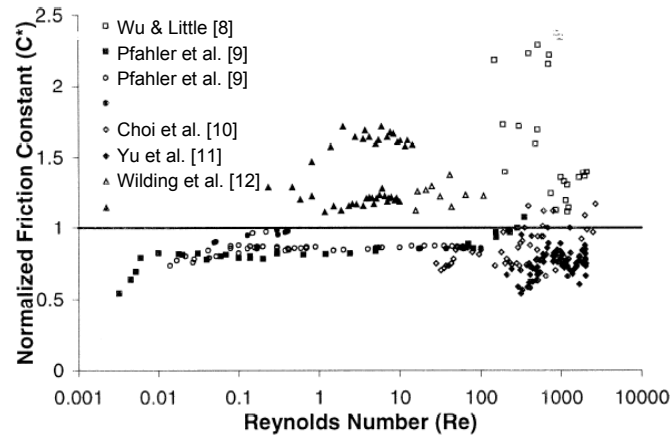
Figure 2.2. Experimental/theoretical friction factor ratio [$C^*=(fRe)_{exp}/(fRe)_{theor}$] as a function of Reynolds Number (adapted from [7]).

An important observation from Figure 2.2 is that each investigator consistently reports numbers higher, lower, or the same as those predicted by theory [7]. From this result, one may conclude that experimental conditions among different experiments are not carefully controlled, and measurement techniques may be in error. Also, some experiments may be performed in a carefully controlled environment, but an analyst is not able to determine which experimental data are free of outside error because experimental data do not match. The data in Figure 2.2 are comparable to most available experimental data, but there exist several explanations why experimental data and theoretical predictions do not match. The results shown in Figure 2.2 are from microchannels of differing geometries, surface roughnesses, materials, conditions and even fluids. This observation is important because experimental conditions among

different microchannel investigations often vary, and this reflects the need for more consistent and clearly documented experimental data.

Mala and Li [13] compared experimental results of water flow in cylindrical microtubes for Reynolds numbers ranging from 100 to 2100. Diameters analyzed ranged from 50μm to 254μm. Mala and Li reported larger friction factors than predicted from a reduction of Navier Stokes, and the difference became larger with decreasing microtube diameter. These effects were attributed to an early transition to turbulence and a change in tube surface roughness. The surface roughness effects were determined by testing with tubes of different material. An effect not considered in this study was the possibility of a longer hydrodynamic entry length for microtubes of smaller diameter.

Wu and Cheng [14] measured friction factor and Nusselt number for laminar water flow in trapezoidal microchannels. Surface roughnesses, surface hydrophilic properties, and channel geometries were varied, and correlations were presented for Nusselt number and friction factor as functions of these variables. The surfaces with different hydrophilic properties were bare silicon and silicon with a 5000Å thermal oxide coating [14]. Ok et al. [15] reported contact angles of liquids on various solid surfaces, and their investigations found a contact angle of 38º for liquid on a thermal oxide coated silicon wafer and a contact angle of 47º for liquid on a silicon wafer. The thermal oxide surface is labeled as more hydrophilic than the bare silicon surface because hydrophilic surfaces have lower contact angles than hydrophobic surfaces. This result implies that the wafer with the thermal oxide coating provides a surface with better wetting characteristics for liquids than the bare silicon surface. There was a

noticeable increase in friction factor and Nusselt number for increased surface roughness, and the more hydrophilic surface (silicon with thermal oxide coating) had a higher friction factor and Nusselt number than the less hydrophilic surface (bare silicon). Both friction factor and Nusselt number were reported to linearly increase with increasing Reynolds number between Re=100 and Re=600, which differs from fully developed Navier Stokes and energy equation predictions.

Several investigators attribute differences between experiment and theory to experimental errors and incorrect reporting of experimental uncertainty. Agostini et al. [16] detailed the importance of obtaining a very low uncertainty when measuring the dimensions of mini and microchannels. An example illustrated that a 3% uncertainty on channel width and height results in a friction factor uncertainty of 21%. Mehta and Helmicki [17] reported that measured pressure drops did not correlate with theoretically predicted pressure drops for laminar flow through microchannels. However, correspondence with the experimenter found that a thin polymer membrane covering the channels deformed under the applied pressure. After this effect was considered and suggested deformation dimensions were substituted into the equations, the theoretical and measured pressure drops matched within 10%.

Additional sources of possible experimental error are:

- Increased pressure drop because of singular pressure losses at the entrance and exit of flow manifolds [16] and because of hydrodynamically developing flow [18]

- Thermocouples can be of the size of microchannels [5]

- The temperature rise of the fluid can be on the order of thermocouple uncertainty [5]

- Trapped gas in liquid microchannel flows can increase pressure drop and decrease Nusselt number [19]

In some cases, theoretical results closely approximated experimental results. Xu et al. [20] measured friction factor for hydraulic diameters ranging from 30 to 344μm and Reynolds numbers ranging from 20 to 4000. For this set of experiments, theoretical predictions matched the recorded data when error ranges from experimental uncertainty were considered.

Toh et al. [18] used the SIMPLER algorithm and a finite volume technique was used to numerically solve the flow, continuity, and energy equations in three dimensions for water flow in a microchannel. The numerical solution was then compared with experimental data for flow in a microchannel of the same geometry. Previously, attempts had been made to validate the experimental results against hydrodynamically and thermally developed Navier Stokes and energy equation predictions, but Toh et al. [18] were the first to model thermally and hydrodynamically developing flow. In addition, velocity and temperature fields for the solid and fluid region were considered. The thermal resistance and friction factor obtained from the numerical results of Toh et al. [18] closely matched the experimental data. The major difference reported was a lower friction factor at low Reynolds numbers. This difference was attributed to lower viscosity as a result of increased mean flow temperature. Toh et al. recommend that

numerical solvers include this in the approximation, though temperature dependence of other fluid properties can be neglected.

Another numerical study by Fedorov and Viskanta [21] solved for fluid flow and conjugate heat transfer in three dimensions for a 57.0μm x 180μm channel using the SIMPLER algorithm with Reynolds number ranging from 50 to 400. Results were compared against existing experimental data. Nearly all numerical predictions for friction factor and thermal resistance matched the experimental data when experimental uncertainty was considered.

Bontemps [5] recently published a figure that shows $Nu_{exp}/Nu_{classical}$ and $f_{exp}/f_{classical}$ as a function of published year from 1990 to 2004. The plot of these ratios shows a clear convergence toward a value of 1 as the years approach 2004. Although this trend is not published in other sources, Bontemps extrapolates from this result that classical (Navier Stokes and energy equations) theories may be applicable on the micro scale [5]. This clear convergence is a possible result of better experimental measurements and techniques with the advancement of time.

As previously mentioned, much of the experimental data from microchannel flow and heat transfer is scattered, and many researchers in this area cite the need for additional experimental data with clear descriptions of experimental conditions and uncertainties before correlations for micro-scale flows are widely accepted.

This work differs from that of Fedorov and Viskanta [21] by using a thermally repeated boundary condition along the z-boundaries; by using the SIMPLE algorithm instead of the SIMPLER algorithm; by obtaining solutions for channels with different

aspect ratios; and by including viscous dissipation when solving the energy equation in the fluid region. Although two analyses of dimensionless parameters including Brinkman number [22 and 23] do not indicate that viscous dissipation will be important for the channel geometries considered, Koo et al. [24] states that viscous heating should be considered for microchannels operating in the laminar regime with hydraulic diameter less than 100μm. The reason for this consideration is because large velocity gradients and long channel length to hydraulic diameter ratios are present in small diameter microchannels. This study includes the viscous dissipation term in the energy equation and makes a comparison to results obtained without the viscous dissipation term.

3. MODEL FORMULATION

Numerical models must be based upon overlying theory and/or assumptions. While the results of the model are dependent upon many factors during the model development, the results cannot provide more insight to the physical phenomena than given by the governing equations and assumptions. Numerical codes are often developed because the governing equations are tightly coupled, nonlinear, difficult to solve, and/or because data used as input to the equations are discrete.

The case considered in this research work is single-phase forced convective flow of water in an array of parallel microchannels. Convection heat transfer is the transfer of thermal energy in the presence of a temperature difference as a combination of bulk fluid motion (advection) and random molecular motion (diffusion) [25]. Since the liquid water is forced through the channels by means of an external pump, the mode of liquid and heat transport is known as forced convection. Velocity components appear in the convective terms of the energy equation, so the solution of the energy equation is dependent upon the converged solution of the flow field.

The density of liquid water does not change appreciably with an increase of temperature, and as a result, mixed convection (free and forced convection) effects are not considered. If gas flows were considered in this study, mixed convection in addition to slip boundary conditions for velocity would likely be included. Since an objective of this study is to compare the numerical results with experimental data, the geometry and experimental conditions will be described, and subsequent discussion will focus on the

equations and boundary conditions that can be used to model the thermohydraulic behavior of liquid water in a microchannel array.

3.1   Description of Experimental Setup of Kawano et al. [3]

The experimental conditions that serve as an origin for the present numerical model are the work of Kawano et al. [3].   Figure 3.1 illustrates the experimental apparatus as used by Kawano et al. [3]. The microchannel device was constructed by etching 110 identical channels centered onto a 15mm by 15mm by 450μm thick silicon substrate. Each channel was 57μm in width and 180μm in height, and the pitch of the channels was 100μm. After the etching, the channels were covered with a 450μm thick silicon cover plate which was etched with holes for connection to the sumps. While the exact method of cover plate attachment is not documented, the two silicon pieces were joined by a molecular diffusion technique [3].
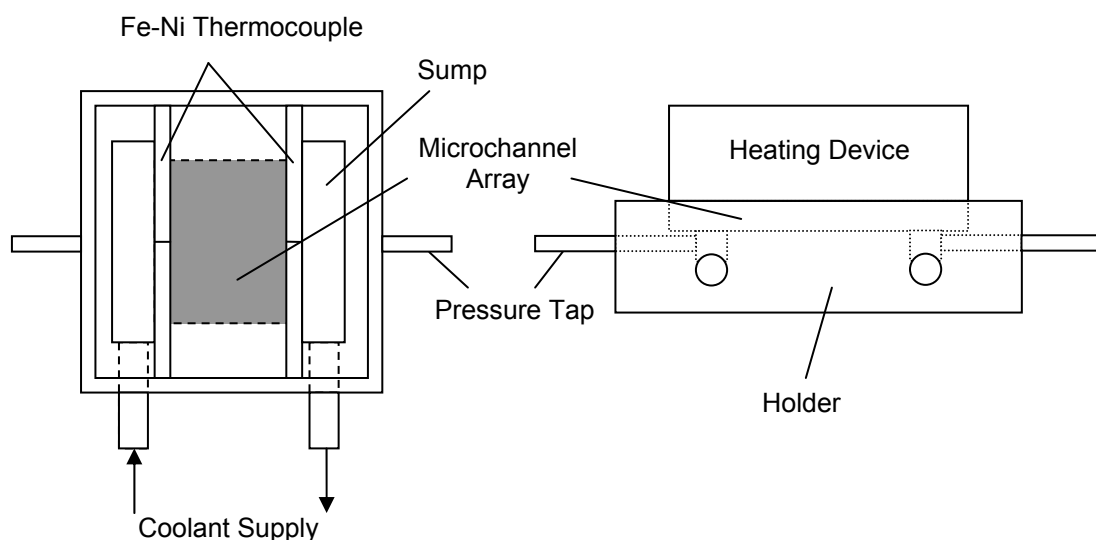
Figure 3.1.   Experimental apparatus for microchannel device (adapted from [3]).

Thin film Fe-Ni thermocouples were created at the inlet and exit of the device by sputtering. These thermocouples allow for measurement of the solid silicon temperature near the channel inlet and outlet. Measurements from these thermocouples will be compared to numerical predictions of temperature in the solid at the same location.

In the experimental work, water was supplied by an external pump to the microchannel device. The microchannel device was housed in a container that allowed fluid connections and pressure measurements to be made at the inlet and outlet sumps. Water flow was controlled by means of a flow meter and a valve for Reynolds number ranging from approximately 50 to 400. A heating device which provided a constant heat flux of 90 W/cm^2 was mated to the side of the microchannel device which is opposite from the flow inlet.

A cross section of one repeating section of the microchannel geometry and the associated boundary conditions are illustrated in Figure 3.2 below. The area shown serves as the model for the initial numerical computational domain. As shown in Figure 3.2, the constant heat flux is applied to the silicon substrate at y = H, and a thermally insulated condition is present at y = 0. Although no insulation was in place at y = 0 during the experiment, this was the location of the holder, and Kawano et al. assumes that this location is thermally insulated [3].

3.2   Geometry

The cross section considered is 100μm wide which is the same value as the pitch of the repeating array, and all microchannels are 10mm long. For the thermal analysis, any repeating cross sectional geometry could be modeled because of the thermally

repeating boundary condition applied in the z-direction. This means that the channel could be centered in the cross section shown in Figure 3.2, and the thermal model would give similar results for temperature distributions within the fluid and solid regions.
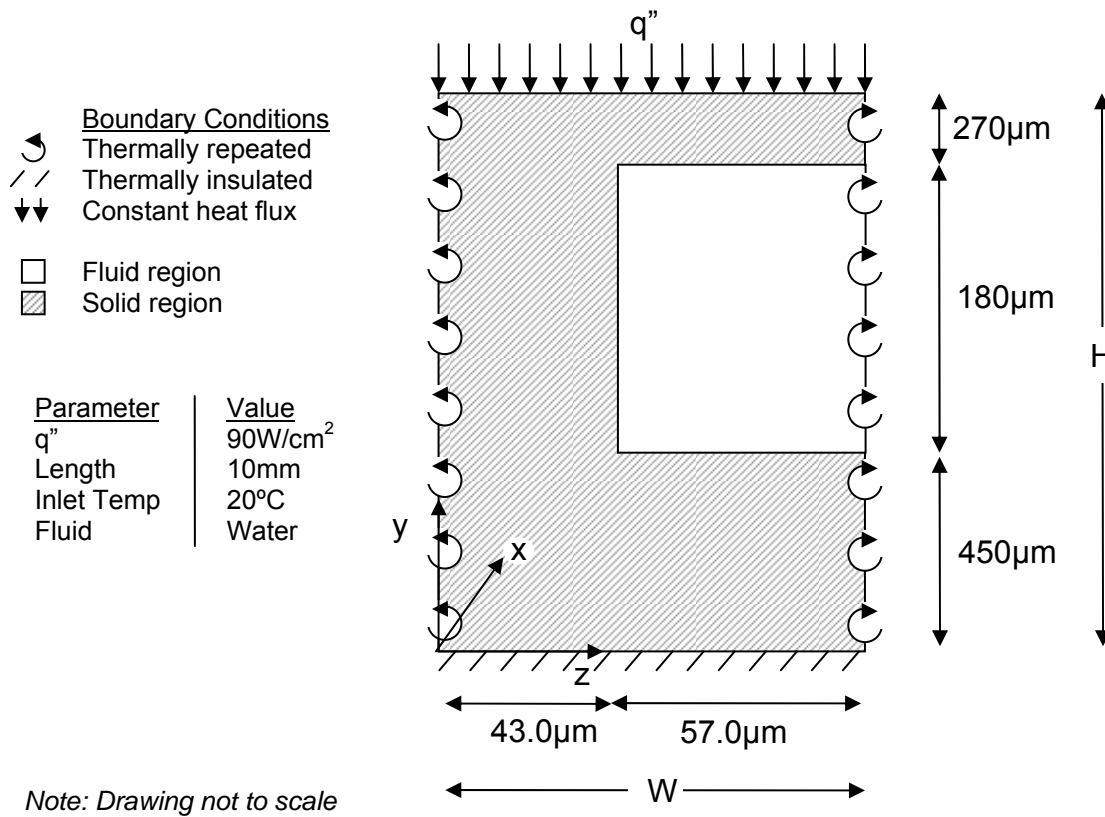
Figure 3.2. Y-Z cross section and boundary conditions for the rectangular microchannel under study.

The case shown in Figure 3.2 has a hydraulic diameter of 86.58μm. Additional geometries are numerically modeled which have the same hydraulic diameter and vertical (y-direction) centering, C, but have different aspect ratios as shown in Figure 3.3. Dimensions for each of the geometries shown in Figure 3.3 are given in

Table 3.1. Each of the geometries shown in Figure 3.3 has the thermally repeated boundary condition applied in the z-direction.
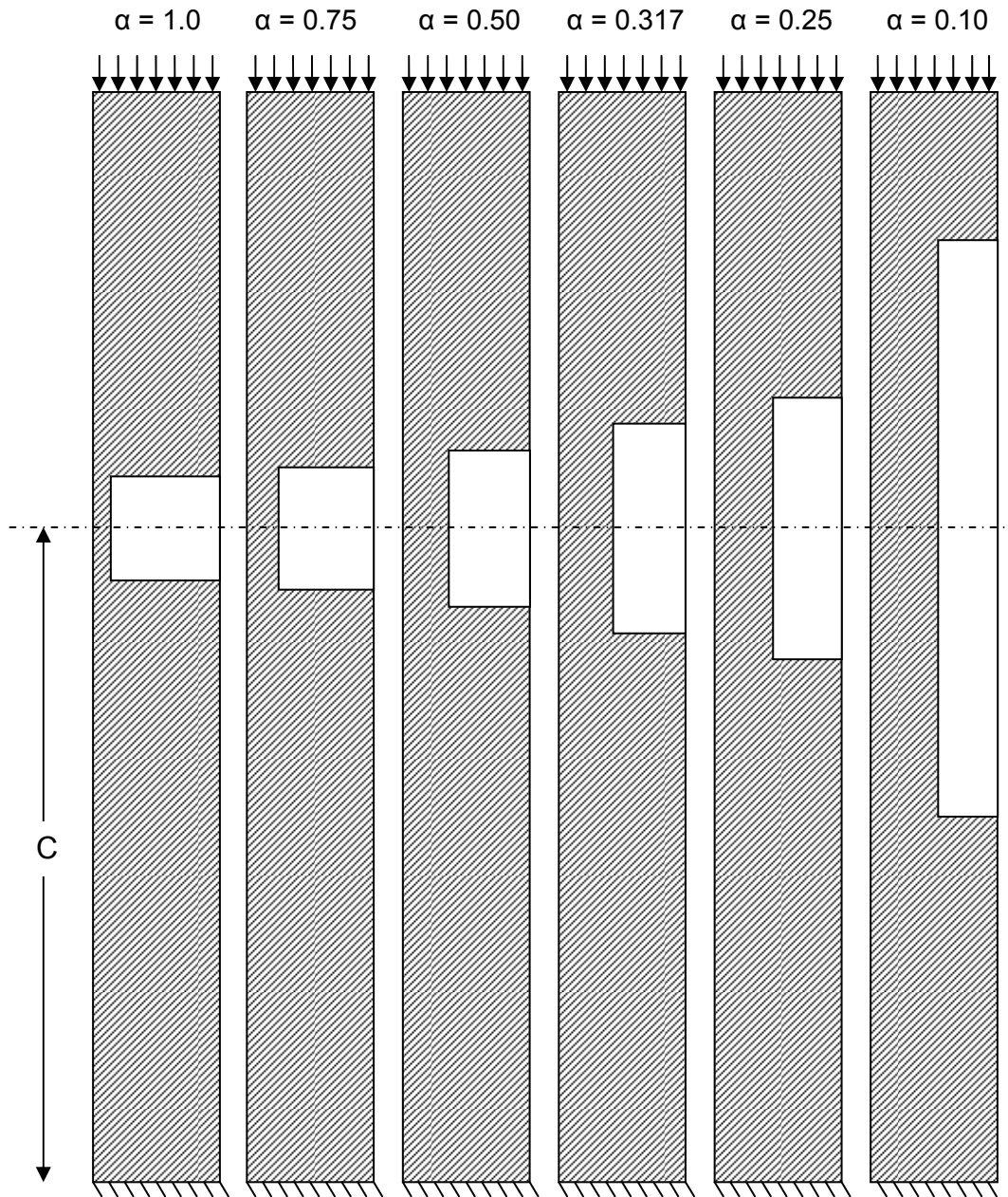
Figure 3.3. Aspect ratios and scale geometries of the six rectangular channels considered.

Table 3.1. Dimensions of channel geometries for cases of different aspect ratio

Aspect Ratio α (w/h)	Channel Height, h (μm)	Channel Width, w_c (μm)	Domain Height, H (μm)	Domain Width, W (μm)	Center Height, C (μm)
0.10	476.2	47.62	900.	100.	431.78
0.25	216.5	54.11	900.	100.	431.78
0.317	180.0	57.00	900.	100.	431.78
0.50	129.9	64.94	900.	100.	431.78
0.75	101.0	75.76	900.	100.	431.78
1.0	86.58	86.58	900.	100.	431.78
The channel length and domain length are 10mm for all cases of aspect ratio.					

3.3 Basic Equations and Boundary Conditions

This study considers laminar forced convection of water, a Newtonian fluid, in an array of silicon microchannels. As shown in Section 2, the dimensions of this problem allow standard continuum hypothesis to be applied while modeling the behavior of water flow in the channels.

The following assumptions were made for the numerical model:

1. Laminar flow

2. Steady state flow and heat transfer

3. Water is incompressible

4. Gravitational forces are negligible

5. Radiation heat transfer is negligible as compared to convection-diffusion heat transfer

6. Buoyancy forces are negligible

7. No internal heat generation is present aside from viscous heating

8. Constant solid properties

9. Fluid properties are dependent on average of outlet and inlet temperatures only, which are a function of Reynolds number when heat flux is constant.

Simulation of fluid flow and heat transfer in a section of the repeated geometry will require the solution of the non-linear three dimensional Navier Stokes equations and the solution to the conjugate (solid and fluid) energy equations. Shah and London [26] indicate that the entry length problem can be solved either by linearizing the momentum equations or by using a finite difference method. Although a more rapidly developing flow is modeled by the linearization method, corrections can be applied to counteract this problem. This method provides a solution for fluid flow in a three dimensional channel, but the velocities in the transverse directions are neglected. This study, however, uses the finite volume method because it provides a better solution for the conjugate heat transfer problem, all velocity components are considered, and the finite volume method is known to give accurate results without the necessity of adding corrections to the model. The finite volume method must use the flow and energy equations in three dimensions as a starting point.

The Navier Stokes, energy, energy source term, and continuity equations for steady-state, incompressible flows in the absence of gravitational forces are given in Eqs. (3.1) through (3.4), respectively, where the S_T term of the energy equation in Eq. (3.2) is equal to the viscous dissipation term as shown in Eq (3.3).

$$\vec{V} \cdot \nabla\left(\rho\vec{V}\right) = -\nabla p + \nabla \cdot \left(\mu\nabla \cdot \vec{V}\right)$$

(3.1)

$$\vec{V} \cdot \nabla\left(\rho c_p T\right) = \nabla \cdot \left(k \nabla T\right) + S_T \qquad (3.2)$$

$$S_T = \mu \left\{ \begin{array}{l} 2\left[\left(\dfrac{\partial u}{\partial x}\right)^2 + \left(\dfrac{\partial v}{\partial y}\right)^2 + \left(\dfrac{\partial w}{\partial z}\right)^2\right] + \left(\dfrac{\partial v}{\partial x} + \dfrac{\partial u}{\partial y}\right)^2 + \\[4mm] \left(\dfrac{\partial w}{\partial y} + \dfrac{\partial v}{\partial z}\right)^2 + \left(\dfrac{\partial u}{\partial z} + \dfrac{\partial w}{\partial x}\right)^2 - \dfrac{2}{3}\left(\nabla \cdot \vec{V}\right)^2 \end{array} \right\} \qquad (3.3)$$

$$\rho\left(\nabla \cdot \vec{V}\right) = 0 \qquad (3.4)$$

The solution to these equations will use the finite volume method and solution technique by Patankar [6] described in Section 4. Because constant fluid properties are considered, the momentum and continuity equations are not dependent upon the energy equation, and the momentum and energy equations may be solved independently. The reverse statement is untrue. The energy equation and source term, Eqs. (3.2) and (3.3), respectively, are dependent upon the velocity field, and for computational efficiency, the velocity field should be determined before the temperature field is solved.

The solution to Eqs. (3.1) through (3.4) is dependent upon the application of boundary conditions, which are graphically depicted in Figure 3.2, and the boundary conditions are the same for all cases, except the value of the entrance fluid velocity. Boundary conditions for velocity include: zero velocity at all y- and z-domain boundary surfaces, uniform x-velocity for liquid at the channel inlet according to Eq. (3.5), zero y- and z-velocities at channel inlet, and zero velocities in the solid region at x=0.

$$u\big|_{x=0,\,fluid\ inlet} = \frac{\mathrm{Re}\,\mu_{fluid}}{\rho_{fluid} D_h} \qquad (3.5)$$

Thermal boundary conditions include: uniform fluid and solid temperature of 20°C at the channel inlet, constant heat flux of 90 W/cm² at y = H for all x and z, thermally insulated at y = 0, and a thermally repeated boundary condition at z = 0 and z = W. The mathematical definition of the thermally repeated boundary condition is given by Eqs. (3.6) and (3.7).

$$T_{z=0} = T_{z=W}$$

(3.6)

$$\left(-k\frac{\partial T}{\partial z}\right)_{z=0^+} = \left(-k\frac{\partial T}{\partial z}\right)_{z=W^-}$$

(3.7)

A thermally repeated boundary condition is one in which the temperatures at the ends of the computational domain are equal only in the direction of repeating geometry, and the heat flux leaving the z = W side of the computational boundary is equal to the heat flux entering the z = 0 size of the computational boundary. This makes physical sense because of the repeating nature of the geometry [27].

The basic channel and solid dimensions given in Figure 3.2 are similar to those used to validate Fedorov and Viskanta's code [21]. Fedorov and Viskanta simulate a different geometry where the fluid channel was centered in the computational domain because an insulated boundary condition was applied in the repeating direction instead of a thermally repeated boundary condition.

The thermally repeated boundary condition is a better depiction of reality compared to an insulated boundary condition because it resembles the repeating nature of the physical geometry. The insulated boundary condition, as modeled in Fedorov and Viskanta's work, is a special case of the thermally repeated boundary condition, which is

true only when the solid region on both sides of the channel are equal in length within the computational domain. In the proposed model, any repeating cross-sectional geometry of constant width in the z-direction could be solved with the application of the thermally repeated boundary condition. For example, the fluid channel could be located at any z-location inside the computational domain shown in Figure 3.2, and the results for the thermal performance of the entire channel array would be identical to the results obtained for any other case. The implementation of a thermally repeated boundary condition differs from the non-thermally repeating cases by using a different line-by-line solver in the repeating direction. The details of the cyclic line-by-line solver are given in Section 4.

The solution is not dependent upon the conditions at the outflow boundary, and no information is carried from the outflow boundary into the computational domain. The gradient of the transport variable, ϕ, in the flow direction, x, is zero at the outflow boundary. This assumes that the flow is hydrodynamically and thermally fully developed at the channel outlet, which is a good approximation because the channel length is approximately 115 times longer than the hydraulic diameter.

3.4   Fluid Properties

The conjugate problem is solved by including the solid and liquid regions in the computational domain for temperature, pressure, and velocity. The solid region is given a very high viscosity ($\sim 10^{45}$) which drives the velocities in this region to a very low value ($\sim 10^{-45}$), and the thermal conductivity in the solid region are equal to the bulk, temperature-invariant thermal conductivity of the solid material. According to

convection-diffusion relationships given in Section 4, when velocity approaches zero, diffusion dominates, which means that conduction is the only method of heat transfer within the solid region.

The assumptions listed in Section 3.3 state that fluid properties are dependent upon inlet and outlet temperatures only, which are a function of Reynolds number in the case of constant heat flux. Since initial tests during the development of the code showed that adding temperature dependent properties increased solution iterations by as much as 300% when compared to constant properties, a different method was employed to determine fluid properties.

From an overall energy balance of the computational domain at steady state, one can determine the outlet temperature of the fluid, as given by

$$T_{m,outlet} = T_{m,inlet} + \frac{q''A_t}{\dot{m}c_p}. \tag{3.8}$$

The average of the inlet and outlet temperatures was used to determine fluid properties, and as these were updated, the inlet velocity changed because of the dependence of velocity on μ_{fluid} and ρ_{fluid} for constant Reynolds number as detailed by Eq. (3.5). Iterations of Eqs. (3.5) and (3.8) were performed until the average of the inlet and outlet temperature ceased to change. Performing the iterations required μ_{fluid}, ρ_{fluid}, k_{fluid}, and $c_{p,fluid}$ to be temperature dependent. These functional relationships were determined for water from available steam tables [25], and the polynomial equations given in Eqs. (3.9) through (3.12) were found to fit the discrete data points very well.

$$\mu_{water}(T) = 2.8665 \times 10^{-11} T^4 - 8.0568 \times 10^{-9} T^3 +$$
$$8.9351 \times 10^{-7} T^2 - 5.2023 \times 10^{-5} T + 1.7432 \times 10^{-3} \tag{3.9}$$

$$\rho_{water}(T) = 1.423 \times 10^{-5} T^3 - 5.7637 \times 10^{-3} T^2 +$$
$$6.3843 \times 10^{-3} T + 1.0002 \times 10^{-3} \tag{3.10}$$

$$c_{p,water}(T) = 3.2760 \times 10^{-6} T^4 - 8.0141 \times 10^{-4} T^3 +$$
$$7.7251 \times 10^{-2} T^2 - 2.9643T + 4.216 \times 10^3 \tag{3.11}$$

$$k_{water}(T) = -8.00 \times 10^{-6} T^2 + .0019T + 0.5687 \tag{3.12}$$

Other than a very high viscosity, the only property that differs in the solid region is the thermal conductivity. The thermal conductivity used for the solid was 148 W/mK, which is the thermal conductivity of single crystal silicon.

4. NUMERICAL PROCEDURE

As shown in the previous section, the equations representing fluid flow and heat transfer in the microchannel are second order partial differential equations. The flow equations are nonlinear and the conjugate nature of the energy problem adds complexity to the energy equation. In such a nonlinear and conjugate problem, no closed form (exact) solution may be obtained for temperature, pressure, and all three velocity components simultaneously, so an appropriate numerical scheme must be implemented.

This work uses the finite-volume technique described by Patankar [6] because of computational accuracy and ease of implementation. This method is also known as the control volume formulation. In a control volume approach, the governing equations are integrated over each control volume so that these equations are satisfied within each control volume, over any quantity of control volumes, and over the entire computational domain. Furthermore, only the unknown values at each nodal point are solved, not the variation between the discrete points [6]. Variations of the transport variable between discrete points are considered locally one-dimensional, and values of the transport variable and fluid properties must be known at each node and control volume face.

4.1 General Transport Equation

A generalized form of the flow and energy equations given in Eq. (4.1) is useful in drawing a similarity among these equations, and the same solution method can be applied to each of these different equations [28]. The solution to Eq. (4.1) requires a technique that accounts for the convective-diffusive nature of the problem. To avoid

confusion, this text uses the term convection-diffusion to represent advection (bulk fluid motion)-diffusion, which is actually convection. The term on the left hand side of Eq. (4.1) represents the convective term, and the terms on the right hand side represent diffusive terms and source terms, respectively. Substituting the variables in Table 4.1 into Eq. (4.1) produces the governing partial differential equations given in Section 3.3.

$$\nabla(\rho\phi\vec{V}) = \nabla(\Gamma_\phi\nabla\phi) + S_\phi \tag{4.1}$$

Table 4.1. Values used in the generalized transport equation for each transport variable, ϕ

Transport Variable, ϕ	Diffusion Coefficient, Γ_ϕ	Source Term, S_ϕ	Equation
1	0	0	Mass Conservation
u	μ	$-\partial p / \partial x$	X-Momentum
v	μ	$-\partial p / \partial y$	Y-Momentum
w	μ	$-\partial p / \partial z$	Z-Momentum
T	k/c_p	Eq. 3.3	Energy

The goal of the numerical procedure is to solve the partial differential equation shown in Eq. (4.1) for a set of discrete points which lie inside the computational domain. The discretization method converts the partial differential equation into multiple series of algebraic equations where the unknowns are the discrete nodal values. When mass, momentum, and energy fluxes are consistent about all control volume faces, Patankar [6] shows that a discretized equation in the form of Eq. (4.2) can be solved provided that all a_i coefficients are positive, S_P is less than or equal to zero, and Eq. (4.3) holds. Subscripts in Eq. (4.2) indicate the location of the neighboring transport variables and coefficients.   Equations (4.4) and (4.5) illustrate the meaning of the source term components shown in Eqs. (4.2) and (4.3).

$$a_P \phi_P = a_W \phi_W + a_E \phi_E + a_S \phi_S + a_N \phi_N + a_B \phi_B + a_T \phi_T + b \tag{4.2}$$

$$a_P = a_E + a_W + a_N + a_S + a_T + a_B - S_P \Delta x \Delta y \Delta z \tag{4.3}$$

$$b = S_C \Delta x \Delta y \Delta z \tag{4.4}$$

$$S_\phi = S_C + S_P \phi_P \tag{4.5}$$

When an equation is transformed from the form of Eq. (4.1) to Eq. (4.2), the a_i coefficients must contain convection-diffusion information as well as the distances between the discrete points. The remainder of this section details the transformation from Eq. (4.1) to Eq. (4.2).

4.2   Discretization Method

Obtaining discretized equations for a given problem first requires selection of the control volume geometry. Typically, one of two different control volume geometries can be considered: control volume faces located directly between nodal points, or nodal points centered in the middle of the control volume. This research work uses the latter formulation because a nodal value in the center of the control volume is a better representation of the transport variable within control volume. Additionally, grid generation is much easier, especially in the case of conjugate and staggered grid problems. Figure 4.1 shows an example of a control volume with dimensions Δx, Δy, and Δz, and it shows the variables and subscripts that appear in this section's equations. The variables δx_i, δy_i, and δz_i are the distances between the central point and the neighboring points.
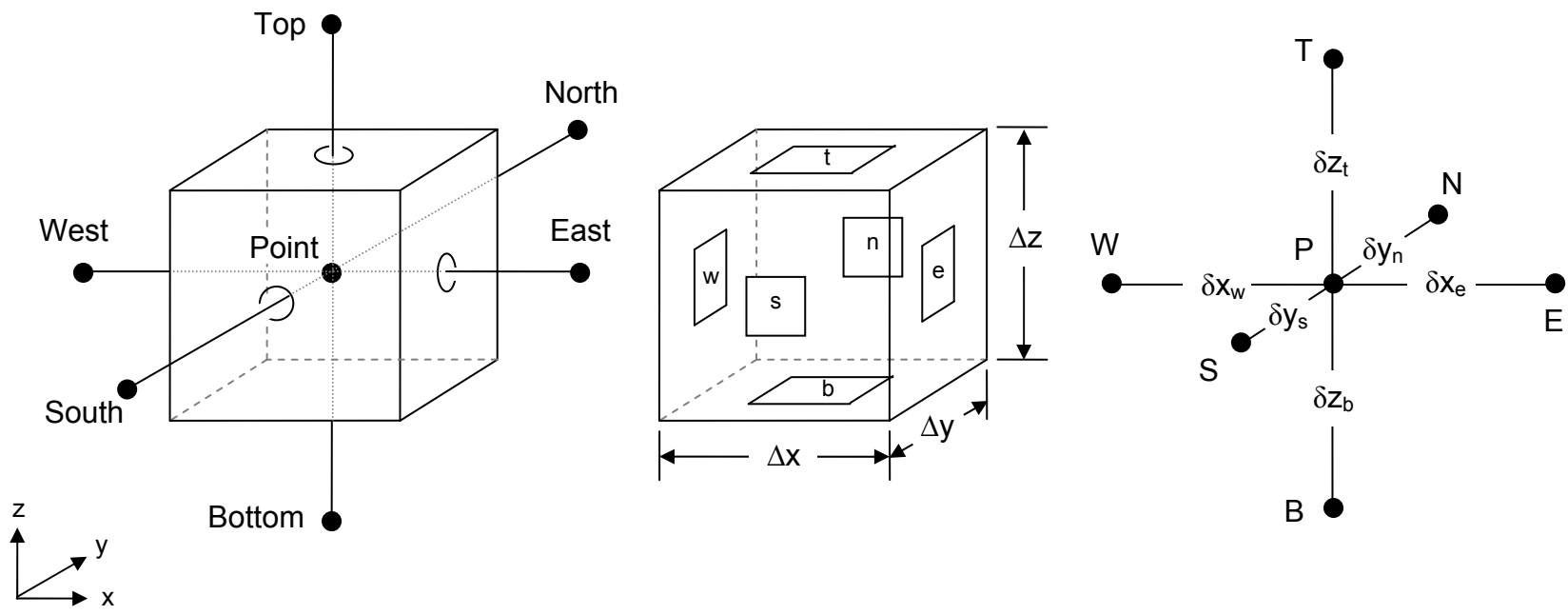
Figure 4.1. Typical control volume with neighboring nodes and variables.

A discretized form of the governing equations can easily be obtained in one dimension, and the results of the one-dimensional solution can similarly be applied in three dimensions. A one-dimensional case of a central node and two neighboring nodes is shown in Figure 4.2 [6]. The control volume illustrated in Figure 4.2 has unit length in both the y- and z-directions.
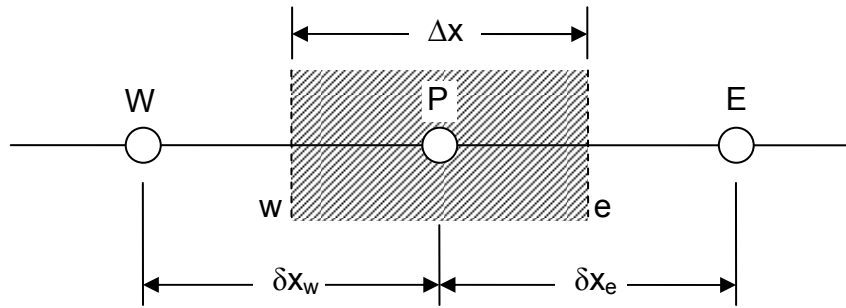
Figure 4.2. One dimensional case for discretizing the generalized transport equation [6].

Equation (4.6) results from integrating Eq. (4.1) without the source term about the control volume shown in Figure 4.2.

$$\left(\rho u \phi\right)_e - \left(\rho u \phi\right)_w = \left(\Gamma \frac{\partial \phi}{\partial x}\right)_e - \left(\Gamma \frac{\partial \phi}{\partial x}\right)_w$$

(4.6)

Grouping the results of Eq. (4.6) by eastern and western faces gives Eq. (4.7). The first term on the left hand side of Eq. (4.7) denotes the total flux of the transport variable at the eastern face, J_e, and the second term denotes the total flux of the transport variable at the western face, J_w.

$$\left(\rho u \phi - \Gamma \frac{\partial \phi}{\partial x}\right)_e - \left(\rho u \phi - \Gamma \frac{\partial \phi}{\partial x}\right)_w = J_e - J_w = 0$$

(4.7)

As shown in Eqs 4.6 and 4.7, values of the transport variable and its derivative must be known at the control volume faces. The definition of these values at the boundary faces requires an assumption to be made about how the transport variable varies between nodal points. Patankar [6] suggests several schemes to be used as solution methods, which include central difference, upwind, hybrid, exponential, and power law schemes. Each of these schemes represents the variables on the left hand side of Eq. (4.7) in terms of nodal quantities.

The scheme for representing the transport variables at control volume faces is one of the paramount issues that must be addressed when discretizing a convection-diffusion equation. For example, if there is a high flow rate from west to east through the control volume in Figure 4.2, the transport variable at the western face of the control volume would have more influence from the western node than from the central node. One simply cannot set the variable at the western face equal to the value at the western nodal point because this methodology would not allow any information to travel from P to W in the case of low flow rates.

In response to the aforementioned problems, Patankar [6] suggests using the power-law scheme to model convection-diffusion behavior at control volume boundaries. The power-law scheme is recommended because it is a very close approximation to the exact solution to Eq. (4.1) in one dimension, and it provides computational savings as compared to the exact solution.

In one dimension, the power-law scheme reduces to Eq. (4.8), which is in the same form as Eq. (4.2). The operator $[|x,y|]$ is equivalent to $\max[x,y]$.

$$a_P \phi_P = a_W \phi_W + a_E \phi_E \tag{4.8}$$

where

$$a_E = \frac{\Gamma_e}{\delta x_e} \left[\!\left[0, \left(1 - \frac{0.1 \delta x_e |\rho u|_e}{\Gamma_e} \right)^5 \right]\!\right] + \left[\!\left[0, -(\rho u)_e \right]\!\right] \tag{4.9}$$

$$a_W = \frac{\Gamma_w}{\delta x_w} \left[\!\left[0, \left(1 - \frac{0.1 \delta x_w |\rho u|_w}{\Gamma_w} \right)^5 \right]\!\right] + \left[\!\left[0, (\rho u)_w \right]\!\right] \tag{4.10}$$

$$a_P = a_E + a_W . \tag{4.11}$$

The values of Γ_i and u_i are evaluated using any kind of interpolation method, but this research work uses the harmonic mean of closest neighbors to calculate Γ_i, and average values of neighboring nodes are calculated for velocity. The definition of harmonic mean is given in Eq. (4.12) below. The reason for this difference is because Γ_i must accommodate step changes between the solid and liquid regions. For example, if Γ_P represents the thermal conductivity in a piece of insulation ($\Gamma_P \approx 0$), then one would expect $\Gamma_i \approx 0$ as in the case of harmonic mean. The numerical average value would only give a value midway between 0 and Γ_E.

$$\Gamma_i = \frac{2\Gamma_P \Gamma_E}{\Gamma_P + \Gamma_E} \tag{4.12}$$

The discretization equation in three dimensions is formed via an approach similar to the one-dimensional formulation. Because the convective and diffusive terms often repeat themselves, it is useful to define the flow and diffusion variables, F_i and D_i, respectively as [6]:

$$F_e = (\rho u)_e \, \Delta y \Delta z \qquad\qquad D_e = \frac{\Gamma_e \Delta y \Delta z}{(\delta x)_e}, \qquad\qquad (4.13)$$

$$F_w = (\rho u)_w \, \Delta y \Delta z \qquad\qquad D_w = \frac{\Gamma_w \Delta y \Delta z}{(\delta x)_w}, \qquad\qquad (4.14)$$

$$F_n = (\rho v)_n \, \Delta x \Delta z \qquad\qquad D_n = \frac{\Gamma_n \Delta x \Delta z}{(\delta y)_n}, \qquad\qquad (4.15)$$

$$F_s = (\rho v)_s \, \Delta x \Delta z \qquad\qquad D_s = \frac{\Gamma_s \Delta x \Delta z}{(\delta y)_s}, \qquad\qquad (4.16)$$

$$F_t = (\rho w)_t \, \Delta x \Delta y \qquad\qquad D_t = \frac{\Gamma_t \Delta x \Delta y}{(\delta z)_t}, \qquad\qquad (4.17)$$

$$F_b = (\rho w)_b \, \Delta x \Delta y \qquad\qquad D_b = \frac{\Gamma_b \Delta x \Delta y}{(\delta z)_b}, \qquad\qquad (4.18)$$

$$P_i = F_i / D_i. \qquad\qquad (4.19)$$

The definition of the power-law scheme is given by Eq. (4.20). Other schemes can be used to represent transport variables at the control volume boundaries by changing the value of $A(|P|)$ in Eq. (4.20).

$$A(|P|) = \left\| 0, \left(1 - 0.1|P|\right)^5 \right\| \qquad\qquad (4.20)$$

Using Eq. (4.20), the discretized equation in three dimensions is represented as [6]:

$$a_P \phi_P = a_W \phi_W + a_E \phi_E + a_S \phi_S + a_N \phi_N + a_B \phi_B + a_T \phi_T + b, \qquad\qquad (4.2)$$

where

$$a_E = D_e A(|P_e|) + \left[\!\left[-F_e, 0 \right]\!\right], \qquad\qquad (4.21)$$

$$a_W = D_w A(|P_w|) + \left[\!\left[F_w, 0 \right]\!\right], \qquad\qquad (4.22)$$

$$a_N = D_n A(|P_n|) + \left[\!\left[-F_n, 0 \right]\!\right], \qquad\qquad (4.23)$$

$$a_S = D_s A(|P_s|) + \left[\!\left[F_s, 0 \right]\!\right], \qquad\qquad (4.24)$$

$$a_T = D_t A(|P_t|) + [\![-F_t,0]\!]$$

(4.25)

$$a_B = D_b A(|P_b|) + [\![F_b,0]\!]$$

(4.26)

$$a_P = a_E + a_W + a_N + a_S + a_T + a_B - S_P \Delta x \Delta y \Delta z$$

(4.3)

$$b = S_C \Delta x \Delta y \Delta z$$

(4.4)

4.3   Staggered Grid

With the nodal points centered within each control volume, the most obvious choice for a grid scheme would be to draw each control volume according to the geometric requirements and place the temperature, pressure, and velocity nodes in the middle of each volume. This method is known as a collocated grid, which is the simplest approach, but this method is not used in this study because potential flaws can arise when obtaining solutions via this method. When velocities, pressures, and temperatures are each defined at the same nodes, pressures and velocities are dependent upon each other at *alternate* grid points rather than *adjacent* grid points. The definition of pressures and velocities at alternate grid points can results in wavy pressure fields and velocity fields, which would not violate any of the discretized equations, but the wavy results would violate physical intuition and the continuous equations that define the fluid flow.

A solution to the wavy velocity and pressure field problems associated with the use of the collocated grid is the implementation of a staggered grid. In this approach, the temperature and pressure nodes are still in the original locations, but each of the velocity grids are staggered in the respective coordinate direction. The staggered grid solution

violates no rules of the control volume method because each dependent variable can have a different grid as long as the volumes within each unique grid are non-overlapping. In the staggered grid approach, the center of the velocity control volumes is located along the face of the pressure/temperature control volume. Another advantage of the staggered grid is that the pressure difference between two adjacent pressure nodes becomes the driving force for the velocity node located at the pressure volume boundary.

The staggered grid presents some difficulty in three dimensions because four different grids must be generated for each computational domain. Each grid has different indexes and coefficients, and boundary conditions must be applied to all grids. Also, properties and dependent variables must be interpolated between nodal values to give results along staggered nodes, which lie on the faces of non-staggered nodes and vice-versa.

A three-dimensional staggered grid is difficult to represent graphically, so a two-dimensional slice is used to illustrate the grid layout. Figure 4.3 shows such a two-dimensional slice, which can be used to represent a slice along a constant z-plane (Case A) or a constant x-plane (Case B). The legend identifies the volumes and nodes for pressure, temperature, and velocity for both cases. Note that the *w*-velocity nodes for Case A and the *u*-velocity nodes for Case B (illustrated by hollow circles) do not lie in the plane of the slice. Rather, they are located midway between the current slice and the next pressure/temperature node. Velocity control volumes are 1.5 times larger along the domain boundaries because the control volumes must be staggered while filling the entire computational domain.
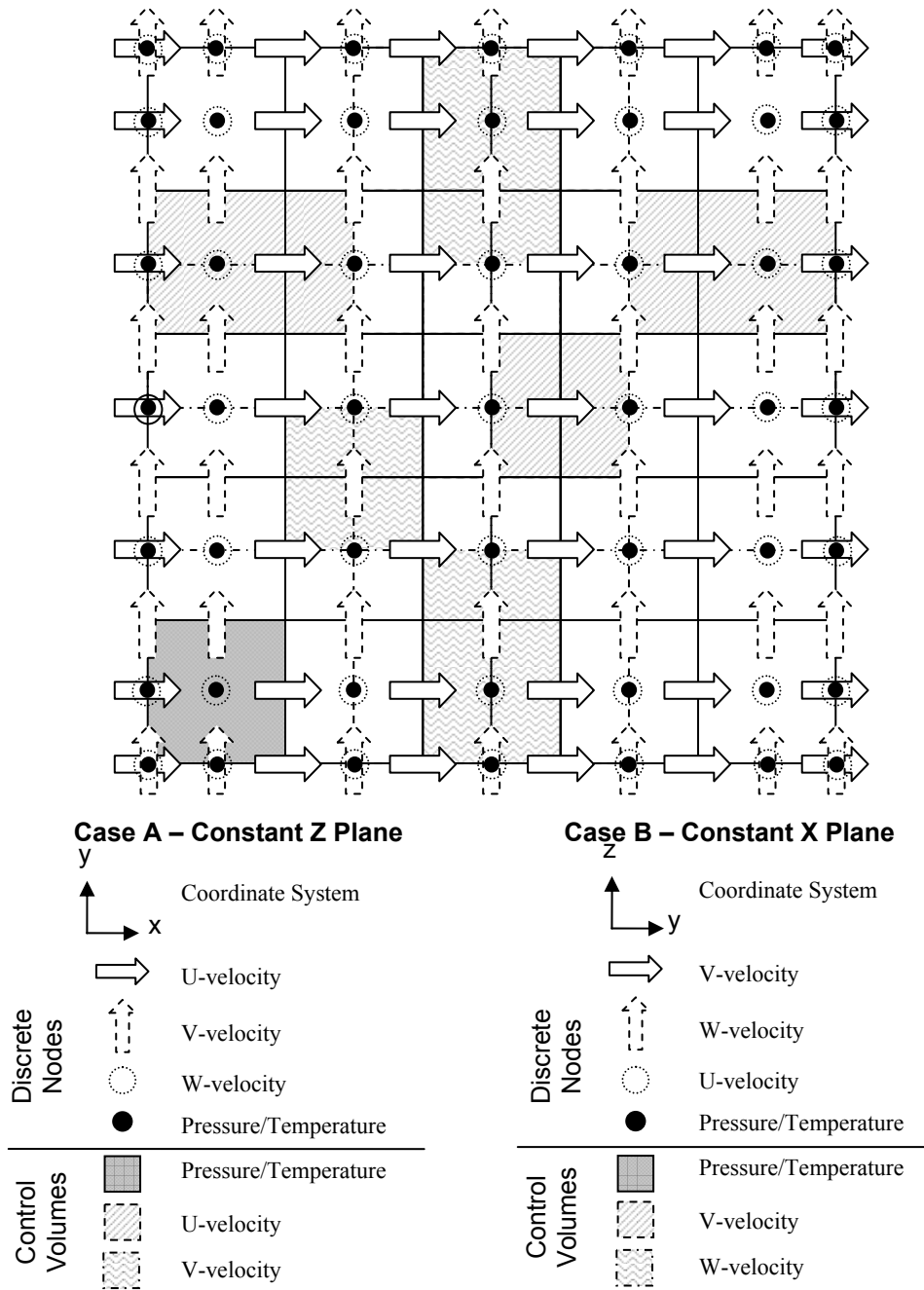
Figure 4.3. Staggered grid in two dimensions.

Figure 4.4 shows a sample of the staggered control volumes in three dimensions. Notice that velocity and pressure control volumes share the same outer faces, but velocity control volumes are 1.5 times larger along the edge. This comes as a consequence of the staggered grid approach. To visualize the entire three-dimensional grid, one should imagine the example volumes spreading from their coordinate axes to fill the entire computational domain.
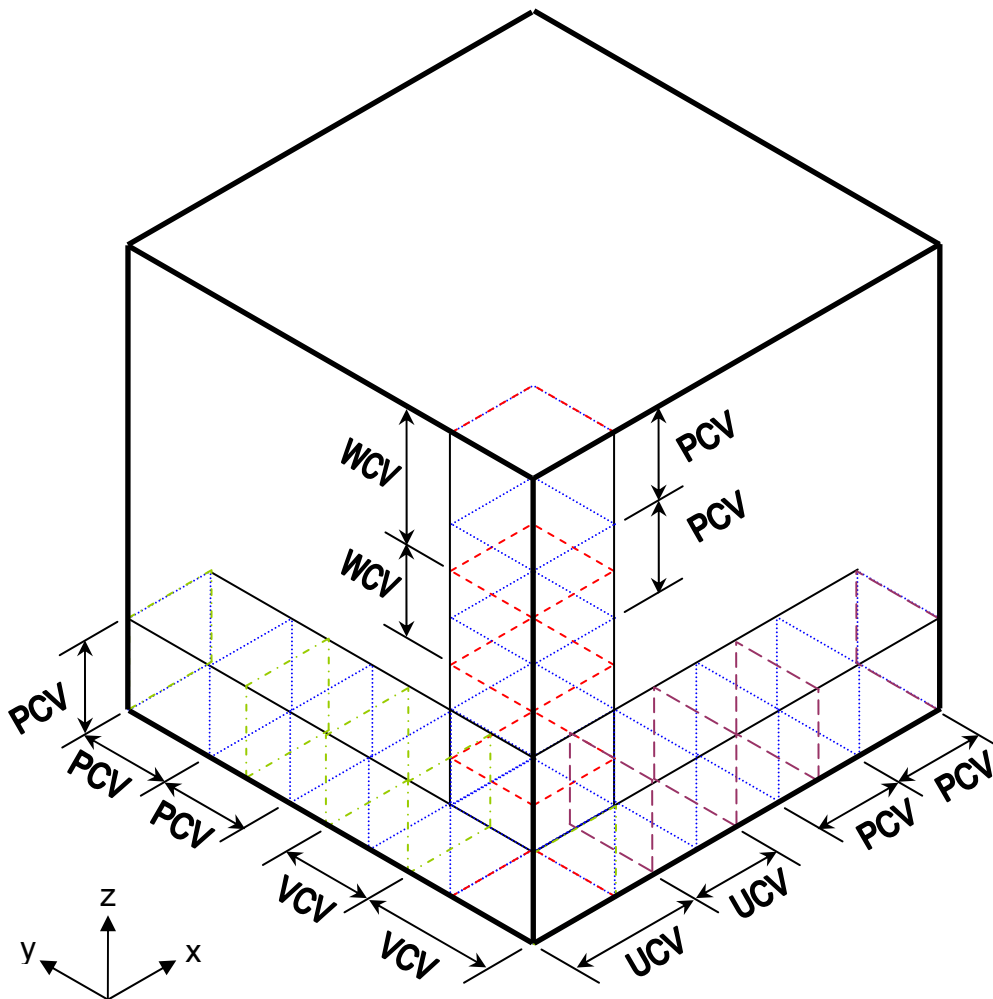
Figure 4.4. Three-dimensional representation of staggered grid and overlapping control volumes (adapted from [29]).

4.4   Solution Algorithm

Although a generalized differential equation and discretized equation for ϕ has been presented, one cannot simply solve these equations with boundary conditions and obtain a correct solution.   The reasons for this are the nonlinearities in the velocity equations and inherent coupling between pressure and velocity.   Recall that Table 4.1 shows pressure difference as a source term in the velocity equations.   Another problem is that internal coupling occurs between each of the velocity components.   If the final converged pressure field was supplied, the velocity and temperature equations could be solved in an iterative fashion to alleviate the problem of internal coupling of velocity components.   Pressure, velocity, and temperature fields must be calculated for given boundary conditions, and a special method is employed to link the pressure and velocity fields.

The solution algorithm employed in this study is the *Semi-Implicit Method* for *Pressure-Linked Equations* (SIMPLE) as described by Patankar [6].   The steps of the algorithm, as given below, provide an iterative procedure for determining the pressure and velocity fields when neither field is specified.   Basically, this method starts with a guessed pressure field; using this pressure field, the velocity fields are calculated.   If the continuity equation is satisfied by the calculated velocity field, then there is no need for additional iterations.   If the calculated velocity field does not satisfy the continuity equation, the pressure field is corrected and the procedure starts over.   The SIMPLE procedure given by Patankar [6] is useful in determining how to apply a correction to the pressure field.

4.4.1 SIMPLE Algorithm Procedure

The procedure followed in this research work for calculating the pressure and velocity fields is the following [6]:

1. Begin with a reasonable guessed pressure field p^*.

2. Using the guessed pressure field, solve Eq. (4.2) for u^*, v^*, and w^* using an appropriate line-by-line technique (as discussed in subsequent sections).

3. Solve for the pressure correction. The pressure correction is obtained by integrating the continuity equation about a pressure control volume and substituting velocity correction factors and velocity values from Step 2. If the pressure correction is zero, then the solved pressure field is the correct pressure field for the velocities obtained in Step 2 and no further pressure correction is necessary.

4. Calculate the new pressure field by adding the pressure correction to the initial guess.

5. Calculate new values for u, v, and w using existing u^*, v^*, and w^* values; $a_P{}^u$, $a_P{}^v$, and $a_P{}^w$ coefficients; face areas of the pressure control volumes; and pressure correction values as shown in Eqs. (4.27) through (4.29) [6].

$$u_e = u_e^* + \frac{A_e}{a_P^u}\left(p_P^{'} - p_E^{'}\right) \tag{4.27}$$

$$v_n = v_n^* + \frac{A_n}{a_P^v}\left(p_P^{'} - p_N^{'}\right) \tag{4.28}$$

$$w_t = w_t^* + \frac{A_t}{a_P^w}\left(p_P^{'} - p_P^{'}\right) \tag{4.29}$$

6. Use the new pressure field as the guessed pressure field and return to step 2. Repeat this procedure until pressure and velocity variables converge.

7. Calculate temperature after converged velocity and pressure fields are obtained. This is done by solving Eq. (4.2) for temperature by the appropriate line-by-line technique in each coordinate direction (discussed in the subsequent sections). In this work, fluid properties are not temperature dependent. Therefore, the flow equations do not depend on temperature. This saves time and computational effort.

4.4.2   Line-by-line TDMA

Steps 2, 3, and 7 of the SIMPLE algorithm require the solution of velocity, pressure, and temperature fields, respectively. With a large system of algebraic equations, one may use either solve them by direct or iterative methods. Direct methods include Gauss elimination and Gauss-Jordan (including matrix inversion). Examples of iterative techniques include Jacobi Iteration, Gauss-Seidel, and Success-Over/Under-Relaxation. Iterative techniques are accurate, but often require many iterations for convergence.

As the discretized equations and coefficients are formed for each node in this study, each grid point depends only on its closest neighbors. For example, grid point (2,1,1) will not depend on (3,6,3), but it will depend on (2,2,1). The consequence of this is that the coefficient matrix will have three values centered along the diagonal and zeros everywhere else. Computational effort would be wasted if the entire matrix were inverted or if an iterative technique were used because each variable is coupled only to

its nearest neighbors. Therefore, a special case of the Gauss elimination method is used to solve the tri-diagonal matrix in one dimension.

When only one dimension is considered at a time, each line can be solved directly by the Tri-Diagonal Matrix Algorithm (TDMA), which is also known as the Thomas Algorithm [30]. This algorithm sweeps the entire computational domain one dimension at a time, and multiple sweeps can be utilized to solve the entire field. Variables in other dimensions that influence a given node are treated as known constants during the solving algorithm, but each variable is updated when the lines it belongs to are solved.

For the three dimensional problem, the line-by-line algorithm solves one line at a time and sweeps the entire cross-sectional domain for a given slice of the third dimension. Once the entire slice has been solved, the next slice in the third dimension will be solved. In this research work, the computational domain is swept by using three sweeping patterns:

- North/south and bottom /top sweep while solving TDMA in x-direction
- West/east and top/bottom sweep while solving TDMA in y-direction
- South/north and west/east sweep while solving TDMA in z-direction

Every time a sweep in the x-direction is encountered, the sweeping direction is from flow inlet to outlet. Sweeping in the opposite direction would not allow information to propagate as easily because the sweep direction would oppose fluid motion. The TDMA algorithm is used to solve all variables in all directions except for temperature in the z-direction. The reason for this difference is because the z-direction

is the coordinate direction of the thermally repeating boundary condition, and this requires the application of a Cyclic Tri-Diagonal Matrix Algorithm (CTDMA).

4.4.3   Line-by-line CTDMA

The solver for the discretized energy equation in the z-direction must differ from the standard line-by-line solver because of the thermally repeated boundary condition in the z-direction only. In this case, an additional algorithm must be used to solve the temperature field in the z-direction. Kim et al. [27] illustrate the need for thermally repeated boundary conditions, and Anand et al. [31] present a Cyclic Tri-Diagonal Matrix Algorithm (CTDMA) that solves the discretized equations in the repeating direction. The CTDMA solver is similar to the TDMA solver discussed previously, but the $z = 0$ and $z = W$ nodes must have the same value, and the heat flux entering control volumes along the face of the $z = 0$ boundary must equal the heat flux leaving the control volumes along the $z = W$ boundary.

An example of the repeating boundary condition in the z-direction is given in Figure 4.5 below. Creation of discretization equations in this dimension results in the matrix shown in Eq. (4.30).
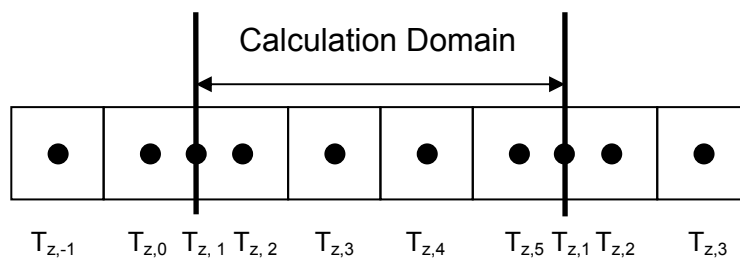
Figure 4.5.   Repeating calculation domain in the z-direction.

$$\begin{bmatrix} a^T_P(1) & a^T_E(1) & 0 & 0 & a^T_W(1) \\ a^T_W(2) & a^T_P(2) & a^T_E(2) & 0 & 0 \\ 0 & a^T_W(3) & a^T_P(3) & a^T_E(3) & 0 \\ 0 & 0 & a^T_W(4) & a^T_P(4) & a^T_E(4) \\ a^T_E(5) & 0 & 0 & a^T_W(5) & a^T_P(5) \end{bmatrix} \cdot \begin{bmatrix} T_1 \\ T_2 \\ T_3 \\ T_4 \\ T_5 \end{bmatrix} = \begin{bmatrix} K_1 \\ K_2 \\ K_3 \\ K_4 \\ K_5 \end{bmatrix} \qquad (4.30)$$

Notice from Eq. (4.30) that each node of Figure 4.5 depends only upon its neighboring nodes. When the thermally repeating boundary conditions are applied, the node to the west of node 1 is equivalent to the western node of node 6 since node 1 is equal to node 6 by Eq. (3.6). Clearly, the application of the thermally repeated boundary condition forces the coefficient matrix to be non-tri-diagonal. The algorithm given by Anand et al. [31] is used in this study because it is capable of solving a matrix that exhibits near tri-diagonal behavior.

4.4.4 *Convergence*

Step 6 of the SIMPLE algorithm states that the entire algorithm must be repeated until convergence is achieved. Often times, convergence is declared by one of three methods: comparison to the true solution, monitoring the residual of each discretization equation, or performing complete mass and energy balances about the entire computational domain.

In this study, convergence is declared by monitoring velocity, pressure, and temperature residuals. Residual equations, $\overline{R}_i$, and convergence criteria, ε_i, are defined in Eqs. (4.31) through (4.33) [32]. The a_i values represent the coefficients for the

variable that is solved for in the discretized equations. Similar residuals were used for v-velocity, w-velocity.

$$\overline{R}_u = \frac{\sum_{nodes} \left| a_e u_e - \sum a_{nb} u_{nb} - A_e \left(P_P - P_E \right) \right|}{\sum_{nodes} \left| a_e u_e \right|} \leq \varepsilon_u \qquad (4.31)$$

$$\overline{R}_p = \frac{\sum_{nodes} \left| \left(\rho_w u_w - \rho_e u_e \right) dydz + \left(\rho_s v_s - \rho_n v_n \right) dxdz + \left(\rho_b w_b - \rho_t w_t \right) dxdy \right|}{\rho u_{ref} L_{ref}} \leq \varepsilon_p \qquad (4.32)$$

$$\overline{R}_T = \frac{\sum_{nodes} \left| a_P T_P - \sum a_{nb} T_{nb} - b_T \right|}{\sum_{nodes} \left| a_P T_P \right|} \leq \varepsilon_T \qquad (4.33)$$

Different values of ε_i were used throughout the code development, but the convergence criteria that were used to declare convergence for each of the geometric cases shown in Figure 3.3 are given in Table 4.2 below.

Table 4.2. Convergence criteria used for non-validation results

Convergence Term	Value
ε_u	10^{-7}
ε_v	10^{-7}
ε_w	10^{-7}
ε_T	5×10^{-8}
ε_p	10^{-5}

5. VALIDATION AND GRID INDEPENDENCE

The main objective of this research is to develop a numerical simulation for predicting flow and heat transfer in a three-dimensional microchannel. Without a method for validating the results and ensuring that they are accurate, there is no way to prove that the results of the numerical simulation are giving realistic and meaningful results. The code is first validated for a different geometry than that shown in Figure 3.3. After the initial validation, a grid independence study was performed for the case shown in Figure 3.3 with an aspect ratio of 0.10 and Reynolds number of 400.

5.1 Initial Validation

A three-dimensional velocity, pressure, and temperature solver utilizing the SIMPLE algorithm [6] was developed as a starting point for this problem. The initial code solved only the fluid region (not a conjugate problem) with standard velocity boundary conditions. Thermal boundary conditions varied among the studies from constant temperature to constant heat flux.

5.1.1 Symmetry

The code was initially verified by solving the flow, pressure, and temperature fields and using strict convergence criteria for velocities, pressure, and temperature for a 10 x 10 x 10 grid size for Re=100. The geometry considered was a square channel of dimensions 20mm x 20mm x 20mm, and constant temperature of 100ºC was used as the thermal boundary conditions on all sides. Properties for air at 25ºC were used.

Throughout this initial validation, convergence criteria given in Table 5.1 were used. Temperature, velocity, and pressure values were symmetric about the y- and z-midplanes to 12 or more significant figures, which verified that erroneous imbalances were nonexistent.

Table 5.1. Convergence criteria used to verify symmetry of numerical results across y- and z-cross sections

Convergence Term	Value
ε_u	10^{-12}
ε_v	10^{-12}
ε_w	10^{-12}
ε_p	10^{-10}
ε_T	10^{-14}

Table 5.2 shows a cross section of temperature data from a z-cross section and a y-cross section. The fifteen significant figures are not important to provide meaningful temperature results, but symmetry in temperature data is an important validation method to use because the temperature equations use the converged velocity field. If there is an imbalance in the velocity field, the resulting imbalance will appear in the temperature distribution throughout a cross section.

Table 5.2. Symmetric temperature distributions in z- and y-cross sections

Z-cross section temperatures (ºC)	Y-cross section temperatures (ºC)
100.000000000000	100.000000000000
69.3930708620383	69.3930708620267
39.4353053302964	39.4353053302788
30.2365790633610	30.2365790633610
28.1235160900451	28.1235160900577
27.7611008603448	27.7611008603622
27.7611008603429	27.7611008603622
28.1235160900348	28.1235160900577
30.2365790633288	30.2365790633611
39.4353053302391	39.4353053302806
69.3930708620011	69.3930708620281
100.000000000000	100.000000000000

5.1.2   Forced Convective Flow Through a Rectangular Channel

Next, a channel was created that was long enough to establish hydrodynamically and thermally fully developed flow. The channel geometry was 3.0mm x 300μm x 100μm, and an evenly distributed grid of 100 x 30 x 10 was used. Later studies showed that this grid could be coarsened considerably in the x and y directions without any considerable change in friction factor or Nusselt number results. Air is used as the fluid in the channel because analytical data was available for hydrodynamic and thermal entry lengths for air and not for water [26].

For a Reynolds number of 100, the hydrodynamic and thermal entry lengths in the 300μm x 100μm channel are 0.735mm and 1.785mm, respectively. Thus, the selection of a channel of length 3.0mm is more than adequate to ensure that the flow is fully developed before the channel exit.

A cross section of the velocities near the channel exit was analyzed and compared to hydrodynamically developed flow conditions reported by Shah and London [26]. Figure 5.1 and Figure 5.2 compare the velocity profiles in the y- and z-directions for the present computation and the analytical approximation. As shown in the figures, the numerical results approximate the analytical approximations quite well.

Following this step, results for the developing entry region were obtained. Values of friction factor and Nusselt number were compared to analytical approximations. The local friction factor, *f*, apparent friction factor, *f*$_{app}$, and Nusselt number, Nu, are defined by Eqs. (5.1) through (5.3).

Figure 5.1. Comparison of present computational results with the analytical solution of Shah and London [26]; x-direction velocity (*u*) profile along y-cross section.
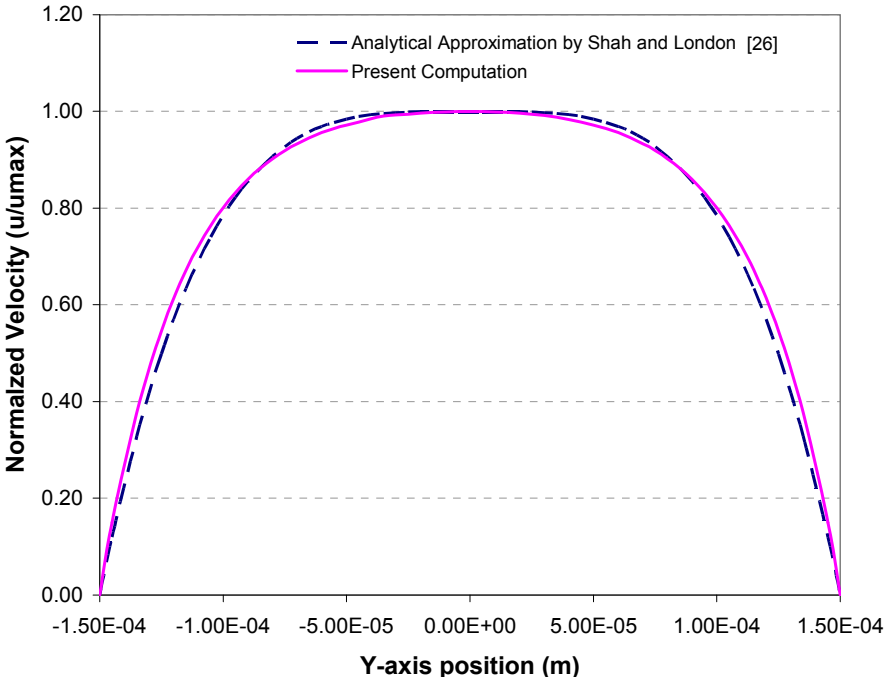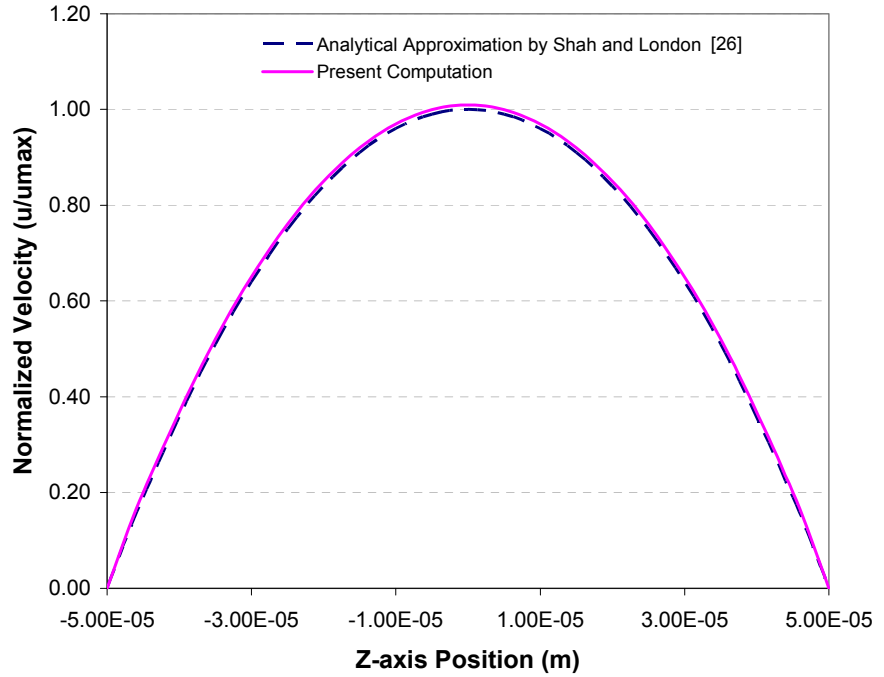

Figure 5.2. Comparison of present computational results with the analytical solution of Shah and London [26]; x-direction velocity (*u*) profile along z-cross section.

$$Po = f \cdot \mathrm{Re} = \frac{2D_h^2}{u_m \mu_{fluid}} \frac{\partial p}{\partial x} \tag{5.1}$$

$$Po_{app} = f_{app} \cdot \mathrm{Re} = \frac{2\Delta p D_h^2}{u_m L \mu_{fluid}} \tag{5.2}$$
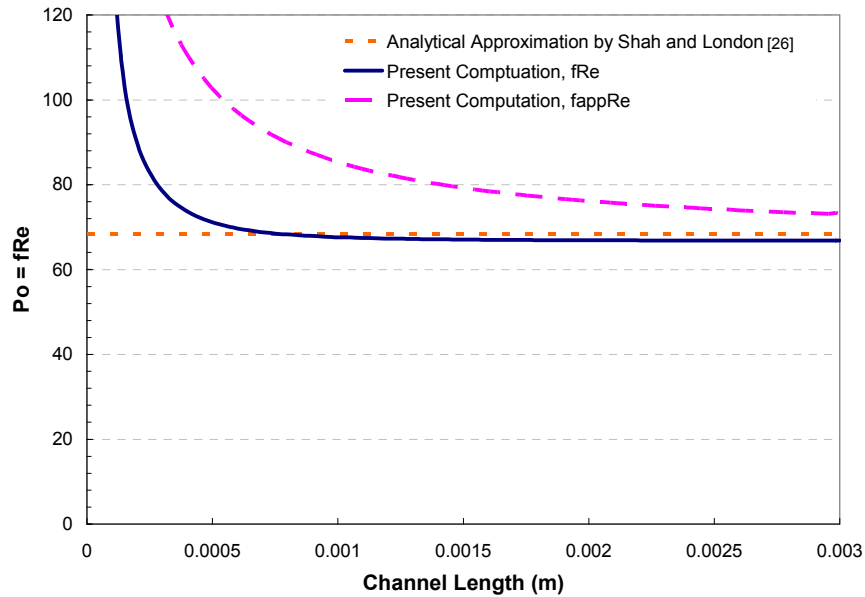
$$Nu = \frac{q'' D_h}{k_{fluid}(T_{w,m} - T_m)} \tag{5.3}$$

where

$$T_{w,m}(x) = \frac{1}{P_s} \int_S T_w(y,z)dS \tag{5.4}$$

$$T_m(x) = \frac{1}{u_m A_c} \int_A u(y,z)T(y,z)\,dy\,dz \tag{5.5}$$

Figure 5.3 compares the numerically determined friction coefficient and apparent friction coefficient with the analytically determined fully-developed friction coefficient. In the fully developed region, the friction coefficients match within 2.3%.

Figure 5.3. Validation of friction factor results as a function of channel length.

Figure 5.4 compares the Nusselt number obtained as a function of channel length from the present numerical code with the analytical thermally developed Nusselt number [26]. The Nusselt numbers match within 0.4% the fully developed region.
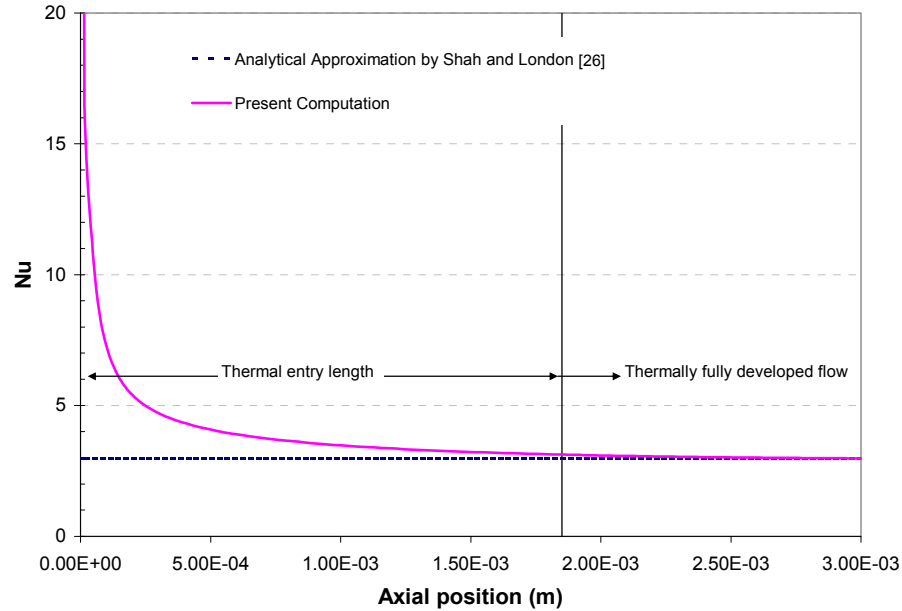
Figure 5.4. Validation of Nusselt number distribution in developing and fully developed regions.

As shown in the comparison and validation figures above, the numerical results favorably approximate well-known theory in the fully developed region. This provides a firm validation and lays the foundation for solving the cases illustrated in Figure 3.3.

5.2 Second Validation

The code was further developed from the geometries used to obtain the initial validations, and the solid regions were added to the computational domain. In addition, the energy equation solvers were modified to allow for constant heat flux at $y = 0$ (insulated) and $y = H$, and the CTDMA line-by-line solver was implemented at $z = 0$ and

z = W for the thermally repeated boundary condition. The fluid properties were changed to those of water and the thermal conductivity of silicon was used for the solid thermal conductivity.

5.2.1 Thermally Repeated Boundary Condition

The thermally repeated boundary condition was validated by considering the geometry shown in Figure 5.5. Thermally repeated boundary conditions were implemented at z = 0 and z = W, and three different cases as shown in Figure 5.6 were solved. The three cases are equivalent to moving the calculation domain about the z-axis of a repeating geometry. If the thermally repeated boundary condition is correctly implemented, then the temperature distributions along the z-direction among the three cases should be shifted but otherwise identical to one another.
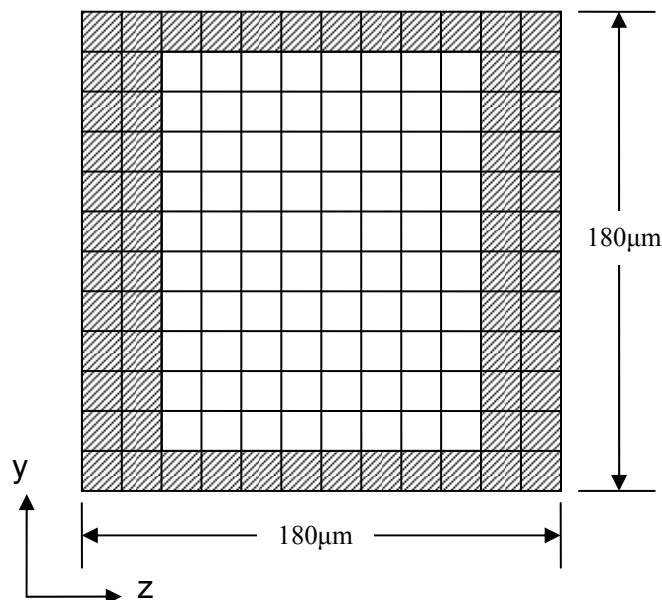
Figure 5.5. Test geometry for validation of thermally repeated boundary condition.
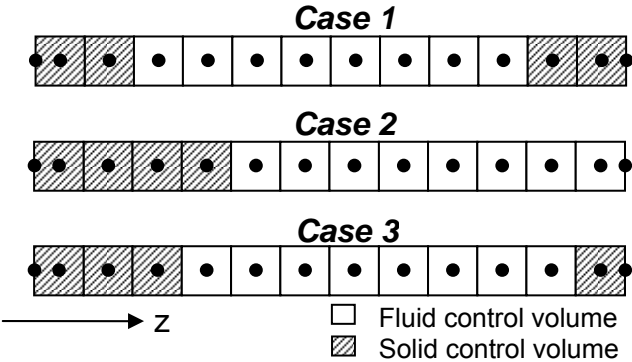
Figure 5.6. Validation cases for thermally repeated boundary condition.

The results of the thermally repeated boundary condition validation are shown in Figure 5.7 below. As shown, the values of temperature at each nodal point appear identical among the three cases except they are shifted, as expected. Also, one can clearly determine the areas of solid and fluid from the temperature distribution.
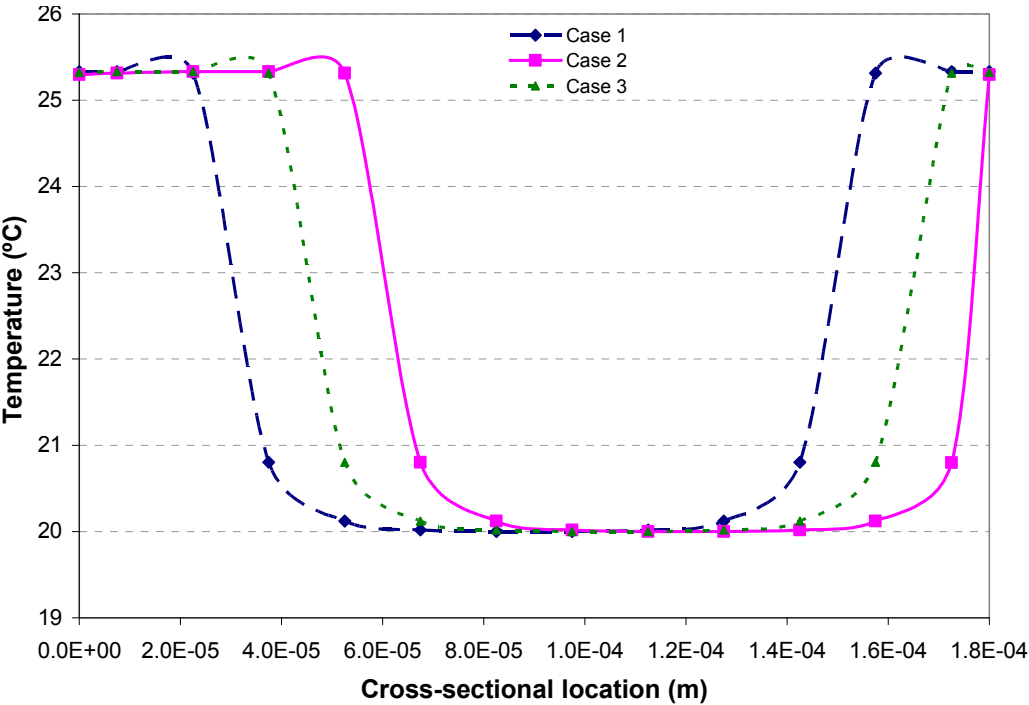
Figure 5.7. Results of thermally repeated boundary condition validation.

Figure 5.8 shows the same results except the data have been translated and superimposed over case 1 data. The only discrepancies occur along the rightmost side at the solid/fluid interface. Consider cases 2 and 3 in Figure 5.6. If cases 2 and 3 are shifted to reflect case 1, there will be an intermediate grid point present because of the zero-thickness control volumes that are present at the z = 0 and z = W surfaces. The curves shown in Figure 5.8 differ only because of the addition of an intermediate grid point. All other points in cases 2 and 3 match case 1 closely.
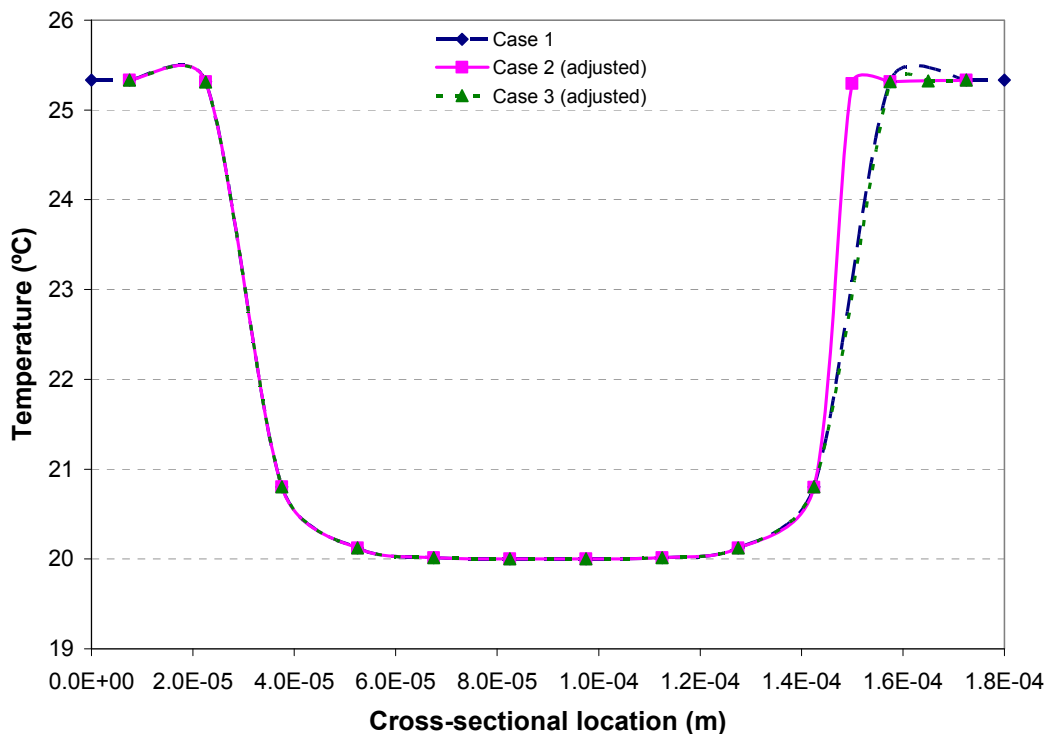
Figure 5.8. Adjusted results of thermally repeated boundary condition validation.

5.2.2 *Energy Balance*

Another validation was used which monitored the overall energy balance for the computational domain. If the energy gained by the fluid is equal to the amount of

energy input into the domain, then there is additional evidence that the flow and energy equation solvers within the numerical code are correct.

The mean temperature of the fluid at the outlet in the numerical study is calculated by Eq. (5.5), and this value is compared to the mean outlet temperature from the energy balance in Eq. (3.8). For the case of 0.317 aspect ratio shown in Figure 3.3 and Reynolds number of 250, the mean fluid temperatures for the numerical computations and the energy balance are given in Table 5.3 below. As shown in the table, the mean outlet temperature values match quite well. Differences could result from a velocity field not being held to very strict convergence criteria and the fact that viscous dissipation is being considered for the numerical computation.

Table 5.3. Comparison of outlet mean temperatures between computation methods

$T_{m,outlet}$, present numerical computation ($^{\circ}$C), Eq. (5.5)	$T_{m,outlet}$, energy balance ($^{\circ}$C), Eq. (3.8)	Percent Difference
28.07	28.01	0.21 %

5.3 Grid Independence Study

After the various validation tests were performed on the code and acceptable results were produced, the code was ready to run the various cases shown in Figure 3.3. Since exact solutions were not known for each of these cases, it was important to perform a grid independence study for the highest Reynolds number case in the worst geometry scenario. The aspect ratio of 0.10 was chosen to be the worst case geometry because it has the largest cross sectional flow area and because of large velocity gradients in the narrow z-direction of the channel. The values of two variables were monitored to declare grid independence. The f_{app}Re value as defined in Eq. (5.2) was

used to monitor behavior of the velocity and pressure fields for the entire channel length, and the outlet thermal resistance value, $R_{t,outlet}$, as defined by Eq. (5.6) was used to monitor the behavior of the temperature field.

$$R_{t,outlet} = \frac{T_{w,outlet} - T_{f,inlet}}{q''} \qquad (5.6)$$

The thermal resistance is an indicator of conduction and convection. For a case of constant thermal conductivity in the substrate and variable flow rate, a low thermal resistance value indicates a high convection coefficient between the substrate and the fluid. Conversely, high thermal resistance indicates relatively weak convective transport. The thermal resistance is also an indicator of maximum substrate temperature since the wall temperature at $y = H$ is used at the channel outlet, which is the location of the maximum substrate temperature.

For a case of constant flow rate and variable thermal conductivity in the substrate, a low thermal resistance would indicate a high substrate thermal conductivity since the temperature gradients would be small, implying a relative insensitivity to fluid temperatures. A high value of thermal resistance would indicate that the substrate acts as an insulator (i.e., low k) since there would be a large difference between inlet fluid temperature and substrate temperature at the channel exit.

Seven different grid sizes were used in the grid independence study, and a non-uniform grid size was used. Since the solid region has zero velocity and a very high thermal conductivity as compared to the fluid, control volumes in the solid region were larger than those in the fluid region. The results of the grid independence study are

shown in Table 5.4 below. According to the results, the percent differences between

cases 5, 6, and 7 are very low. Therefore, case 5 is declared as grid independent.

Table 5.4. Tabulated results of the grid independence study

Case	X	Y	Z	Number of Nodes	% diff	$f_{app}Re$	% diff	$R_{t,outlet}$	% diff
1	100	44	8	35200		80.397		7.164×10^{-2}	
2	105	54	9	51030	44.97	82.504	2.62	7.191×10^{-2}	0.368
3	110	60	11	72600	42.27	83.791	1.56	7.203×10^{-2}	0.175
4	115	70	13	104650	44.15	84.674	1.05	7.218×10^{-2}	0.197
5	120	84	15	151200	44.48	85.702	1.21	7.232×10^{-2}	0.201
6	123	90	16	177120	17.14	86.020	0.371	7.237×10^{-2}	0.0622
7	125	105	17	223125	25.97	86.051	0.0360	7.231×10^{-2}	0.0801

Values of Δx, Δy, and Δz for case 5 were used to solve the other geometries of

different aspect ratio shown in Figure 3.3. The values of Δx, Δy, and Δz are given in

Table 5.5. The first 100 nodes within the first 4mm use the Δx value shown in Table 5.5,

and after the first 4mm, Δx increases at a rate of 16% per node until the channel exit is

encountered. Smaller control volumes are used in the first 4mm so that all entry length

effects are simulated correctly. The values of velocity, pressure gradient, and

temperature gradient are constant after the entry region, so a coarser grid is used.

Furthermore, velocities are zero within the solid region and temperature gradients are

small compared to those in the fluid region so a coarser grid is also used in the solid

region. Each solid control volume bordering the fluid region was given the same size as

those in the fluid region so that accurate temperature and velocity gradients would be

obtained. In case 5, 10 solid control volumes were used in the y-direction and 5 solid

control volumes were used in the z-direction.

Table 5.5. Control volume lengths used in case 5 of the grid independence study

Solid Region		Fluid Region	
Δx	40	Δx	40
Δy_{north} / Δy_{south}	59.10 / 38.49	Δy	6.435
Δz	14.29	Δz	4.762
All control volume dimensions are in μm			

6. RESULTS AND DISCUSSION

The basic equations presented in Section 3 and the numerical procedure presented in Section 4 were used to create a FORTRAN computer code that solves for u, v, and w velocity fields, pressure field, and temperature field in three dimensions. The code was used to solve these fields for each of the geometries shown in Figure 3.3 as Reynolds number was varied between 50 and 400. Other values such as friction coefficient, mean temperature, and thermal resistance were calculated once the converged velocity, pressure, and temperature fields were obtained.

6.1   Comparison with Experimental Data

As stated in Section 1.2, one of the objectives of this work is to compare the apparent friction coefficient and thermal resistance values obtained from the computational results with available experimental data [3]. The geometry used to gather experimental data is shown in Figure 3.2, and the numerical computations used this same geometry. Equations for apparent friction coefficient and outlet thermal resistance are given by Eqs. (5.2) and (5.6), respectively. The equation for inlet thermal resistance is given by Eq. (6.1), where $T_{w,inlet}$ is defined as the substrate temperature at y = H at the channel inlet.

$$R_{t,inlet} = \frac{T_{w,inlet} - T_{f,inlet}}{q''} \qquad (6.1)$$

As the outlet thermal resistance is an indicator of thermal conductivity and convection coefficient, the inlet thermal resistance gives the same values on a different

scale. For substrates with high thermal conductivity, $T_{w,inlet}$ and $T_{w,outlet}$ will have similar values, and the inlet and outlet thermal resistances will be similar. Inlet and outlet thermal resistances will be dissimilar for substrates with low thermal conductivity. Local convection coefficients are larger at the channel inlet than at the channel outlet because of entry effects, and the inlet thermal resistance conveys information about the convection coefficient. When more thermal energy is transferred to the fluid near the channel entrance, the substrate temperature near the channel entrance will decrease and the thermal resistance will be lower. If less thermal energy is transferred to or from the fluid near the channel entrance, the convection coefficient will be lower, which will increase the substrate temperature near the channel entrance and, consequently, the thermal resistance will be higher.

The comparison of apparent friction coefficient values between the present numerical study and the experimental work of Kawano et al. [3] is shown in Figure 6.1. The comparison shows good agreement between the experimental results and the present numerical computation when experimental uncertainty is considered. The uncertainty range of these experimental data varies between 12% and 15%. In the range of Reynolds number studied, the variation of apparent friction coefficient is linear. This result differs from the fully developed friction factor results which are often used as a basis of comparison for laminar flows in microchannels. For the geometry considered, the fully developed flow friction coefficient is 69.2 [26], which does not match the data for Reynolds number above 250.

The linear increase of apparent friction coefficient with increasing Reynolds number is explained by the increasing hydrodynamic entry length. Throughout the entry region, the flow is not developed and velocity gradients are large, which lead to increased pressure drop. When the entry region increases in length with increasing Reynolds number, a higher pressure drop will be evident within the channel. The local friction coefficient values are equal to the fully developed flow friction coefficient values for all Reynolds numbers in the laminar regime. The present numerical results are nearly identical to the numerical results of [21] and [33], for the same geometry and boundary conditions.
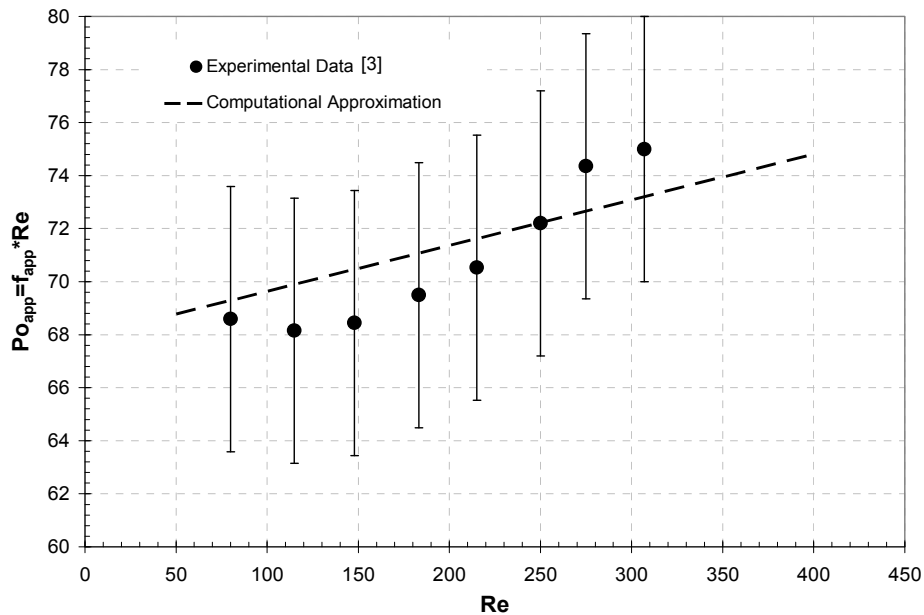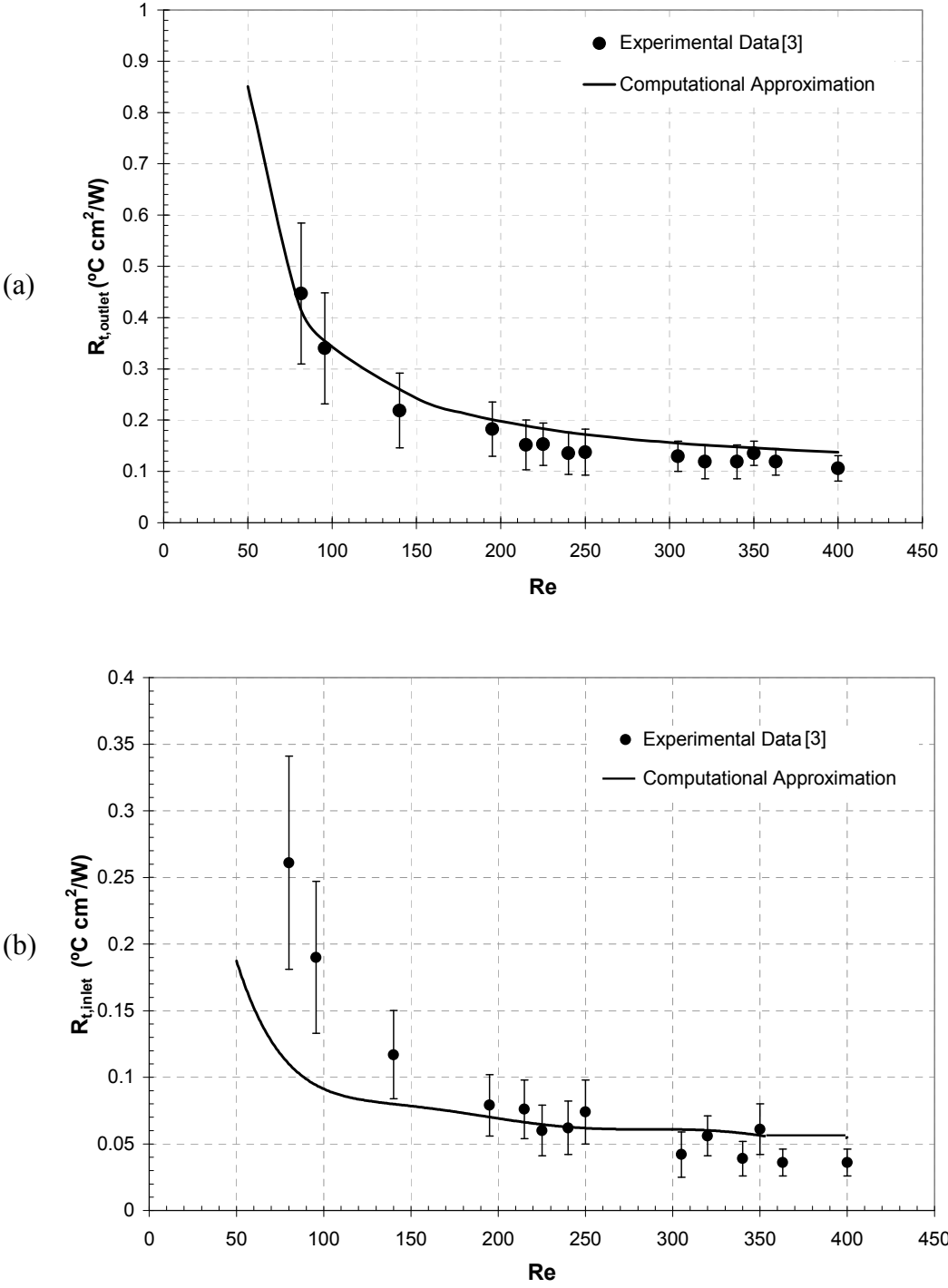

Figure 6.1. Comparison of present computational results of apparent friction coefficient with the experimental data of Kawano et al. [3], α=0.317.

Many experimental investigations of microchannels cite early transition to turbulence because of increasing friction coefficient with increasing Reynolds number. For the case of Reynolds number considered, the entrance length can be on the order of

10-20% of the channel length [26]. For higher Reynolds numbers within the laminar regime, the entrance region may extend beyond the channel length. The extension of the entrance region would bring about much higher friction coefficients than those predicted by fully-developed laminar flow correlations.

Inlet and outlet convective thermal resistance are shown in Figure 6.2. The numerical and experimental data for the outlet convective thermal resistance match quite well when uncertainties are considered. The inlet convective thermal resistance values differ for low Reynolds number flows, and the numerical model under-predicts the thermal resistances obtained experimentally. Qu et al. [33] suggest that this difference could be a result of heat loss to the upstream plenum because substrate temperatures are higher for low Reynolds number flows. In addition to the friction coefficient data, the numerically obtained results for convective thermal resistance in this study match those obtained by [21] and [33] very closely. The thermal resistance values obtained in the present study slightly over-predict those given by Fedorov et al. [21], whose results tend to fall in the ranges of the lower error bars shown in Figure 6.2*a*.

Figure 6.2. Comparison of present computational results of convective thermal resistance with the experimental data of Kawano et al. [3], α=0.317 at (a) the channel exit and (b) the channel inlet.

6.2   Numerical Results for All Geometries

As previously discussed, the velocity profile at the entrance is uniform, and it takes a finite length before the velocity profile becomes fully developed (not changing with length). Figure 6.3 shows the developing velocity profiles for both the y- and z-cross sections at the channel midlines for a Reynolds number of 400 and aspect ratio of 0.10.   The velocity profile appears flat in the y-direction for fully developed flow because the channel is ten times longer in the y-direction than in the z-direction. Thus, the velocity profile is largely influenced by the narrow z-direction. From Figure 6.3, one can see that the flow is hydrodynamically fully developed at approximately 11% of the channel length, or 1.1mm. The solid region is shown in these figures to emphasize the fact that the solid region was included in the computational domain and to provide the reader with a sense of scale.

As the apparent friction coefficient was compared with experimental data for an aspect ratio of 0.317 in Figure 6.1, the apparent friction coefficients for all aspect ratios considered in this study are given in Figure 6.4. The friction coefficients for other aspect ratios have the same general trend as the case for 0.317 aspect ratio. In Figure 6.4a, the slope of the f_{app}Re vs. Re lines are nearly identical for each aspect ratio, and they only differ by translating to a higher f_{app}Re value as the aspect ratio decreases. This makes intuitive sense because a fluid in a channel of smaller aspect ratio will have higher velocity gradients than in channels with larger aspect ratios. From Figure 6.4b, there is a smaller difference among f_{app}Re values for all Reynolds numbers considered when the aspect ratio becomes smaller.
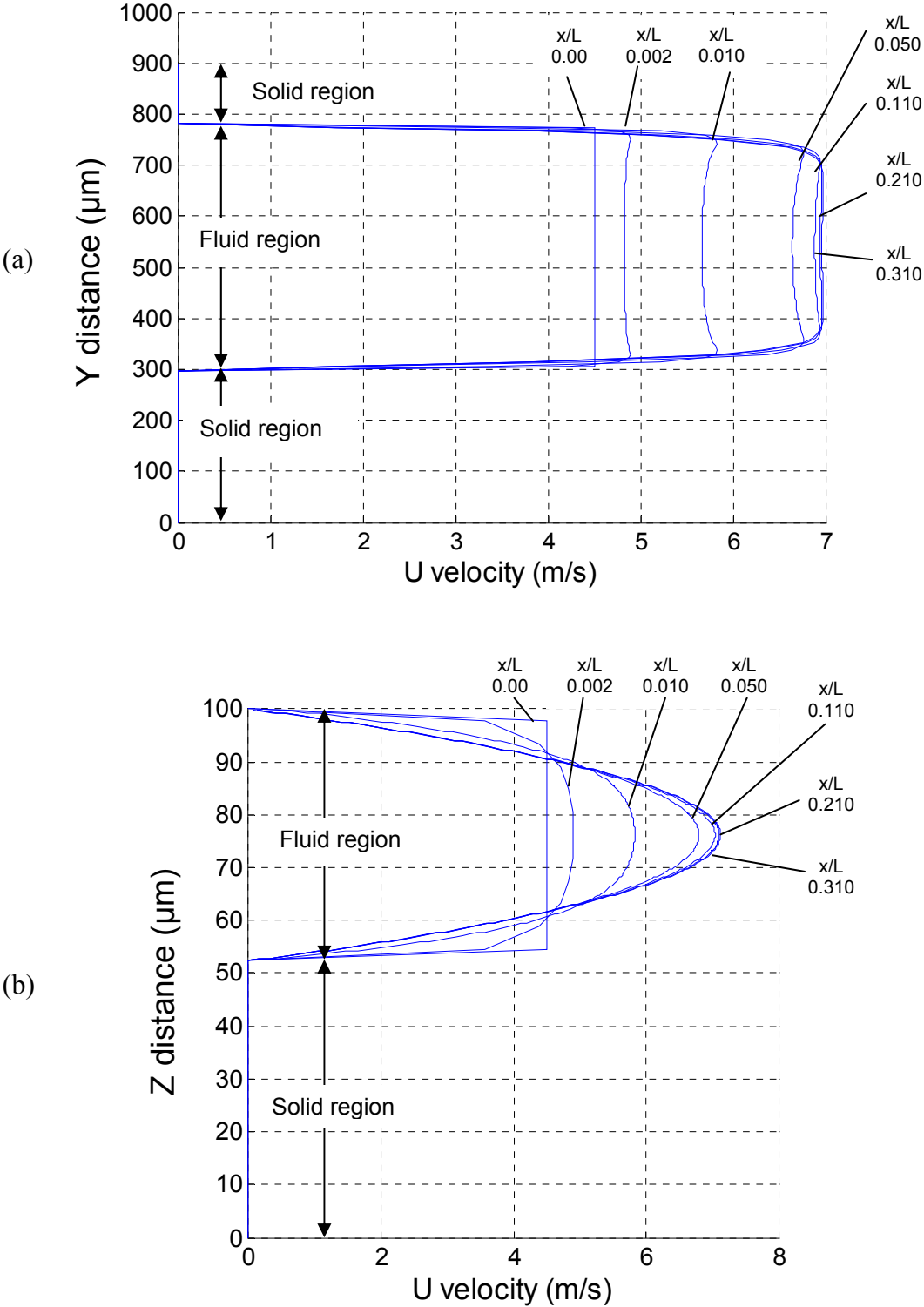
Figure 6.3. Developing velocity profiles for Re=400 for α=0.317 for (a) y- and (b) z- cross sections.
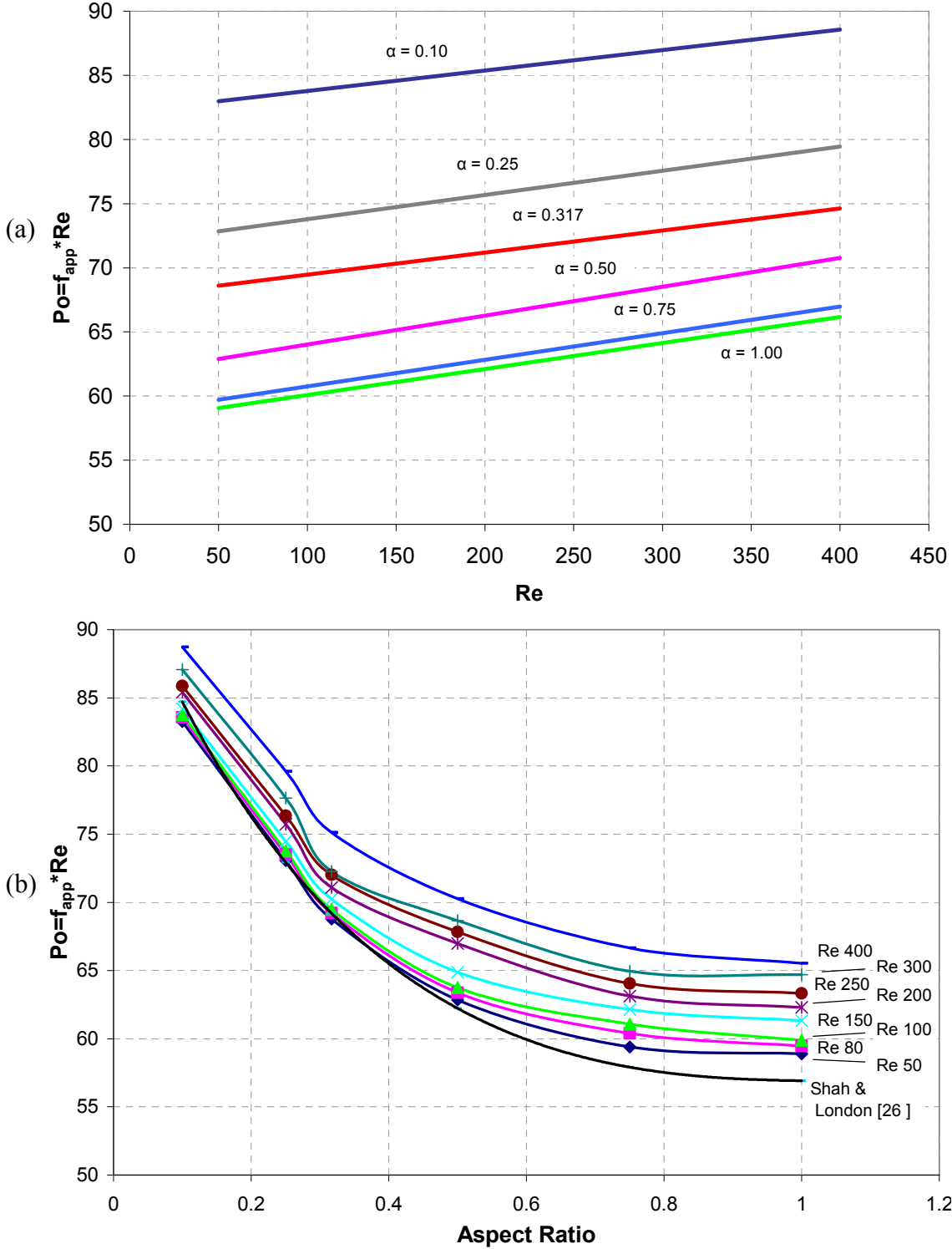
Figure 6.4. Apparent friction factor (a) versus Reynolds number for various aspect ratios (b) versus aspect ratio for various Reynolds numbers.

As cited in Section 1.1, a motivation for this work is to serve as a predictor for flows in microchannels so that external systems may be designed for optimum performance. In most microchannel experiments, a flow loop must be constructed to provide a constant temperature fluid to the microchannel device, which requires knowledge of the pressure drop across the microchannel array. Although the microchannels are not long compared to macro-sized channels, the small hydraulic diameters cause short microchannels to have very large pressure drops for laminar flows.

Using the data from the pressure fields, the pressure drop across a single channel was determined for each flow rate and geometry. The flow rate per channel was multiplied by the number of channels in the array (110), and the system characteristic curves shown in Figure 6.5 were produced. These characteristic curves could be used for selecting an appropriate pump for flows in the microchannel array.

For a given flowrate, the 0.10 aspect ratio channel has a lower pressure drop compared to all other channels. This is an important result because the 0.10 aspect ratio channel has the largest apparent friction coefficient but the lowest pressure drop for a given flow rate even though all channels have the same hydraulic diameter (Figure 6.4a and Figure 6.5). The pressure drop information could also be computed from the f_{app}Re data given in Figure 6.4 by using the relationship given in Eq. (5.2).
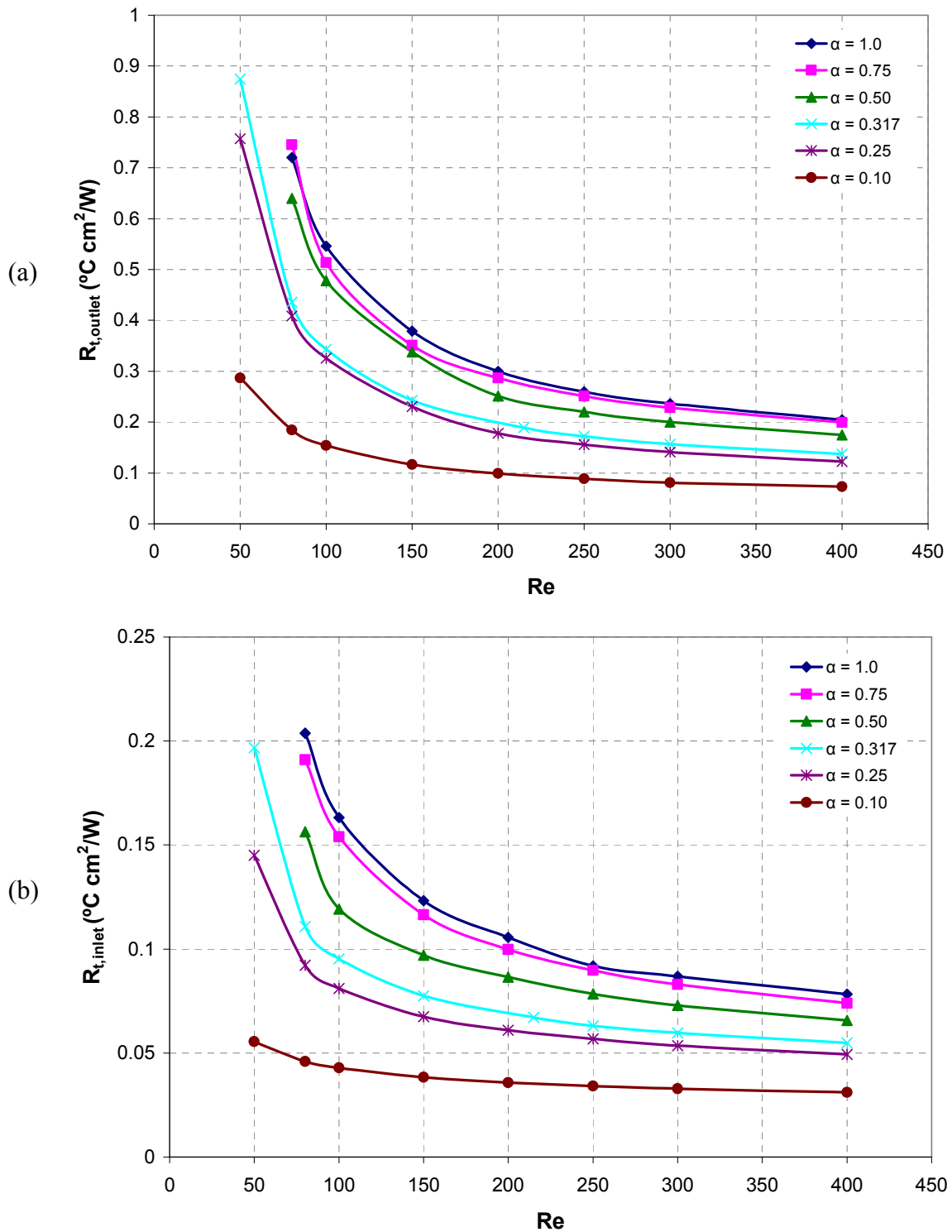
Figure 6.6 shows values for convective thermal resistance at both the channel outlet and inlet for all Reynolds numbers and aspect ratios considered. This figure serves as a useful tool for understanding the substrate temperatures as a function of channel geometry and water flow rate. At low flow rates, substrate temperatures can

become very high as evidenced by the high values of thermal resistance at low Reynolds number and high aspect ratios. In these results, thermal values for Re = 50 are not provided for aspect ratios 1.0, 0.75 and 0.50 because energy balance calculations indicated that the fluid would reach boiling temperatures. Boiling of liquid flows in microchannels has been the topic of many investigations, but it is not considered in the present study.

For high Reynolds numbers, the substrate temperatures become very close to the liquid inlet temperatures. This allows us to extrapolate that the microchannels can dissipate heat loads larger than 90 W/cm^2 for Reynolds number beyond 400 before substrate temperatures reach very high values.
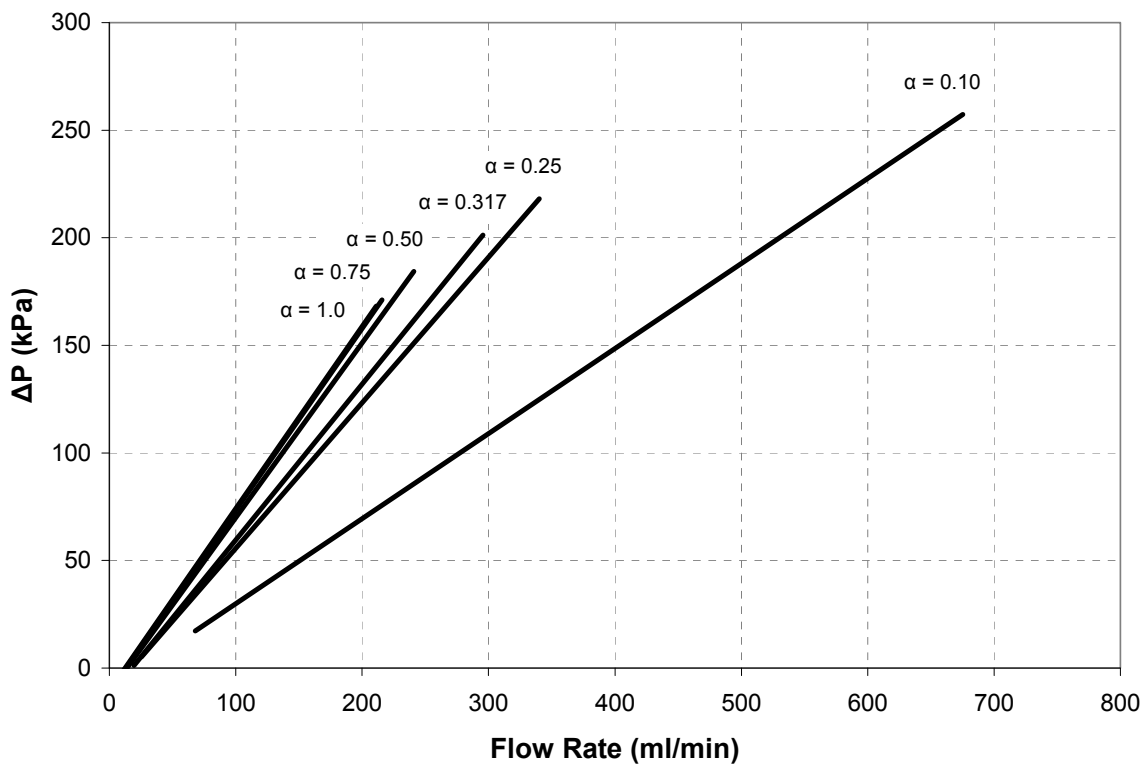
Figure 6.5. System characteristic curves for the entire array of 110 parallel microchannels.

Figure 6.6. Comparison of convective thermal resistance values for all cases of aspect ratio vs. Reynolds number at (a) the channel exit and (b) the channel inlet.

The mean fluid temperature is shown in Figure 6.7 as a function of channel length and Reynolds number for the aspect ratio of 0.50. With the exception of the short thermal entry length, the flow is thermally fully developed for over 95% of the channel length for all Reynolds numbers considered. Downstream of the entry length, the mean fluid temperature is a linear function of x, and values of the mean fluid temperature at the channel exit are consistent with those obtained by a system energy balance as given by Eq. (3.8). In this study, the mean fluid temperature distribution for all aspect ratios can be approximated as linear between the inlet and the outlet temperature as predicted by Eq. (3.8).
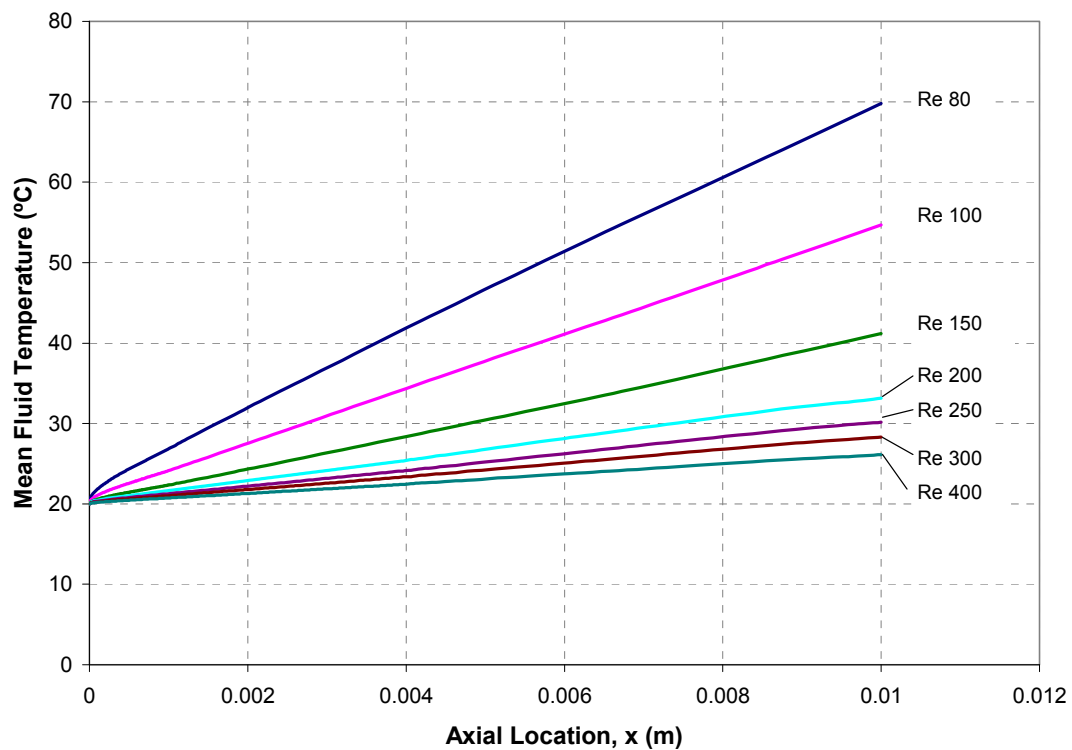
Figure 6.7. Mean fluid temperature distribution along channel length for Reynolds number ranging from 80 to 400 and α=0.50.

Figure 6.8 shows the maximum silicon substrate temperatures for each case of Reynolds number and aspect ratio. This is an important consideration because the maximum substrate temperature occurs at the location of the heat source, which is the location of the integrated circuitry or a heater. Knowledge of the maximum temperature allows the system designer to avoid high-temperature operating conditions and to calculate thermal stresses. For small aspect ratios, the substrate temperature does not vary greatly as a function of Reynolds number. Larger aspect ratio channels have high maximum substrate temperatures for low Reynolds numbers. Increasing Reynolds number beyond 200 does not have a large effect on the maximum substrate temperature for any particular case of aspect ratio.
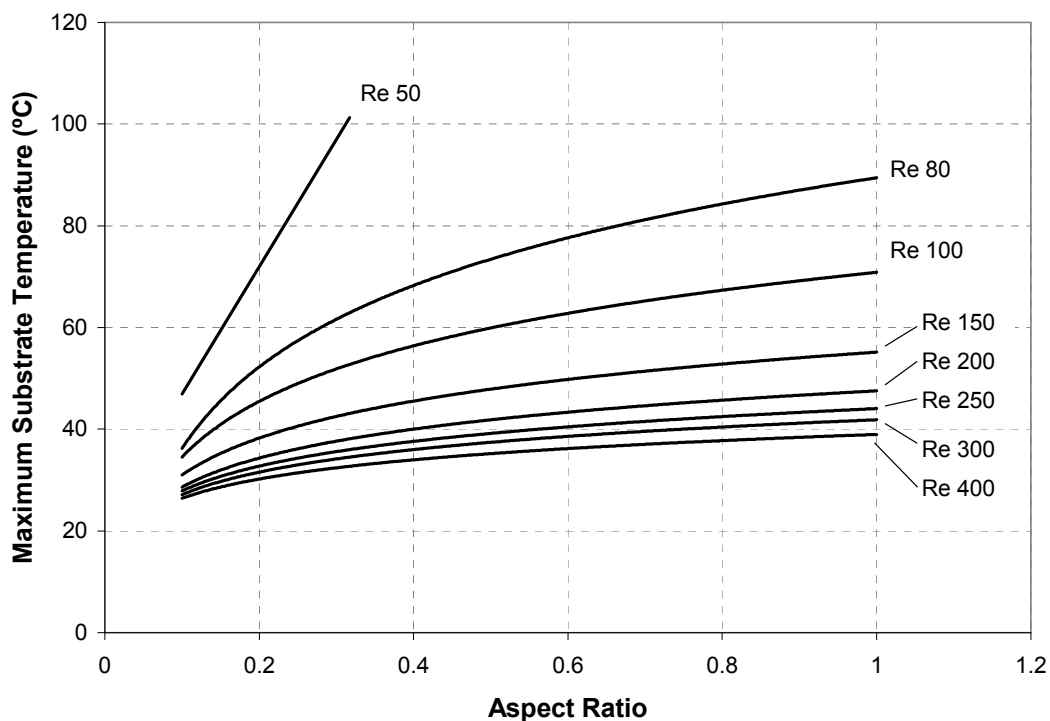
Figure 6.8. Maximum silicon substrate temperature as a function of aspect ratio for Reynolds number ranging from 50 to 400.

Temperature contour plots for slices within a 0.10 aspect ratio channel are given in Figure 6.9 and Figure 6.10 for a silicon substrate and a copper substrate, respectively. The contour plots are the only location that thermal results are displayed for a copper substrate. Copper was considered because of its very high thermal conductivity and as a tool to illustrate the transfer of thermal energy within the solid. Each of the slices through the fluid channel occurs at the location of the channel midplane.

The thermal boundary conditions implemented on the computational domain can be seen clearly for the Re = 100 case shown in Figure 6.9. The y = 900μm boundary shows a temperature gradient that results from the constant heat flux boundary condition. The y = 0 boundary shows no temperature gradient, which is indicative of the thermally insulated boundary condition. Fluid temperatures along the lower y-boundary of the channel (south wall) are lower than the substrate temperature. This means that the thermal energy travels from the heat source to all sides of the fluid channel. The temperature distributions show a large temperature gradient in the fluid along the lower y-boundary of the channel. This means that a non-trivial amount of energy is transferred to the fluid along the lower y-wall.

The temperature distributions shown in Figure 6.10 indicate that there is better heat spreading as a result of the higher thermal conductivity. The *average* substrate and fluid temperatures appear to be the same between the silicon and copper cases, but the temperature difference of the substrate between the outlet and the inlet is smaller for the copper case than for the silicon case. The effect of this is that the inlet thermal

resistance is increased and the outlet thermal resistance is decreased for the copper substrate as compared to the silicon substrate.

The temperature distribution of the liquid in the copper microchannel shows a lower temperature gradient in the y-direction than compared with the liquid in the silicon microchannel. This is not a surprising result because the thermal energy spreads more widely in the copper substrate, and the solid region at the south end of the channel has attained a higher temperature by way of conduction. The copper substrate allows for nearly identical temperature gradients of the fluid along the north and south walls, implying that the amount of heat transferred at the top and bottom walls are comparable to one another. Also, because of the better heat spreading in the copper, the maximum substrate temperature is reduced.

The last objective of the current study is to analyze the effect of viscous heating. Since viscous heating terms include velocity gradients, high Reynolds number flows in geometries that cause large velocity gradients will more likely exhibit viscous heating than other cases. These factors became the impetus for choosing $Re = 400$, $\alpha = 0.10$, and $\alpha = 1.0$ for the viscous heating study. The mean fluid temperature as a function of channel length was calculated for each case. Figure 6.11 compares the numerical results for the cases of viscous heating and non-viscous heating for the $\alpha = 0.10$ case. In this case, the mean fluid temperatures differ by only 1.76% at the channel exit when viewed relative to the inlet temperature.
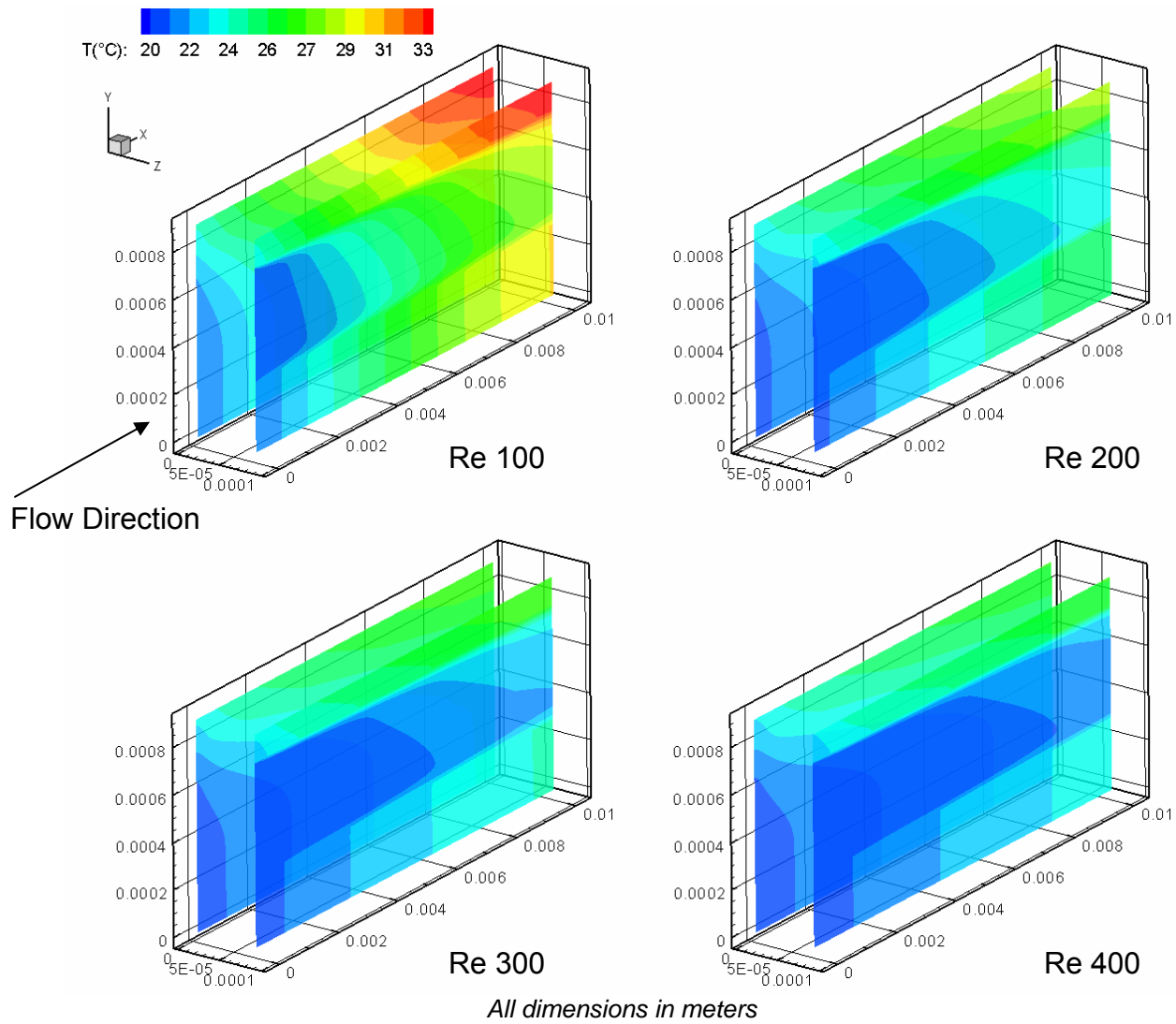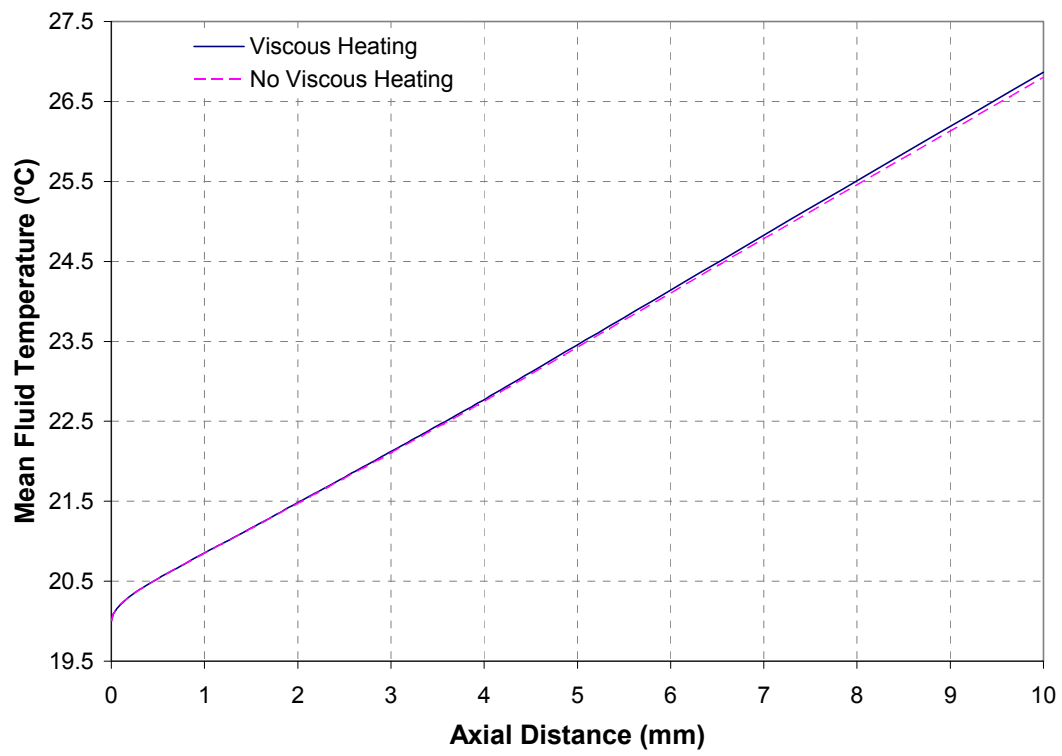
Figure 6.9. Temperature distributions along selected slices within channel of 0.10 aspect ratio, silicon substrate.

Figure 6.10. Temperature distributions along selected slices within channel of 0.10 aspect ratio, copper substrate.
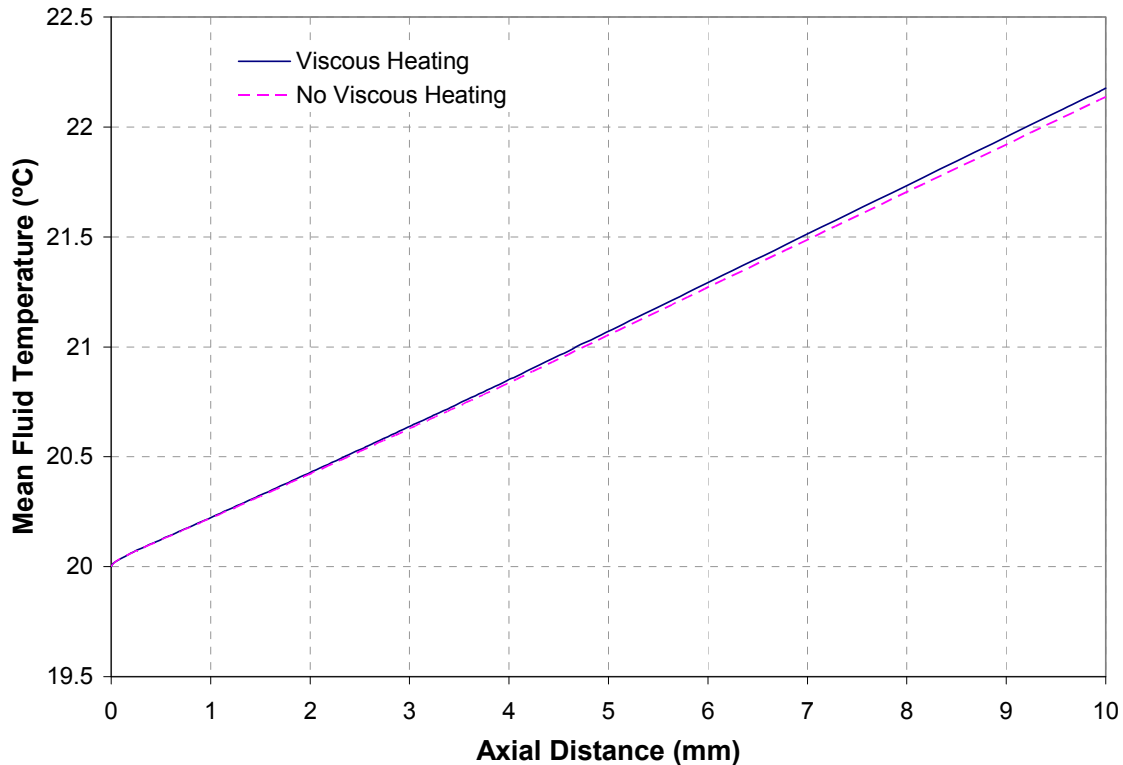
Figure 6.11. Comparison of mean fluid temperature distributions with and without viscous heating considerations for Re=400 and α=0.10.

Figure 6.12 shows the mean temperature as a function of channel length in a channel of α = 1.0 for the viscous heating and non-viscous heating cases. The mean fluid temperatures of the viscous heating and non-viscous heating cases differed by 0.98% when temperature difference between inlet and outlet was considered for each case. From these results, it is evident that viscous heating is not an important consideration for channels considered in this study, but the effect of viscous heating may need to be considered for much longer channels or channels of very small hydraulic diameter or small aspect ratio. Clearly, the channel with a higher aspect ratio exhibited a higher temperature rise than the channel of large aspect ratio.

Figure 6.12. Comparison of mean fluid temperature distributions with and without viscous heating considerations for Re=400 and α=1.0.

7. SUMMARY

A numerical study was executed which simulated three dimensional fluid flow and heat transfer in a repeating section of a microchannel array. The conjugate nature of the heat transfer problem added complexity, and a thermally repeated boundary condition was implemented to accurately model the repeating nature of the geometry. The three dimensional Navier-Stokes and continuity equations were solved using the SIMPLE algorithm, and once a converged velocity field was obtained, the three-dimensional convection-diffusion energy equations were simultaneously solved in both the solid and fluid regions. Rectangular microchannels with a hydraulic diameter of 86.58μm were studied as aspect ratios varied from 0.10 to 1.0 and Reynolds numbers ranged from 50 to 400. The following conclusions were made:

1. The continuum hypothesis holds for liquid flows in the channel sizes considered, and Navier-Stokes equations with no-slip boundary conditions can be applied to model the cases considered.

2. In this study, the linearly increasing friction coefficient that was observed between Reynolds numbers 50 and 400 is a result of increased hydraulic entrance length.

3. This model is a valid model for the 0.317 aspect ratio case because friction factor values and convective thermal resistance values closely matched experimental data [3]. As the convective nature of the problem is dependent

upon velocity fields, the closeness of the thermal resistance values to the experimental data lends credibility to the numerical model.

4. It is assumed that thermohydraulic results for other aspect ratios are legitimate because hydraulic diameter was not changed between the case validated against experimental data and because the continuum assumption holds.

5. Viscous heating need not be considered for the cases of geometry and Reynolds number considered in this study. Only a channel with smaller cross-sectional dimensions, higher Reynolds number flows, or much longer length would require consideration of viscous heating.

6. Increasing the thermal conductivity of the substrate allows for increased heat spreading, reduces the maximum substrate temperature, and equalizes the amount of heat transferred along the northern and southern channel walls.

7. Mean fluid temperature along the channel length may be approximated from a standard energy balance for a single repeating channel geometry.

8. For the same hydraulic diameter, inlet and outlet thermal resistances and friction coefficient values change very little for aspect ratios larger than 0.50. Values of inlet and outlet thermal resistance decrease for aspect ratios approaching 0.10. Friction coefficient values monotonically increase for aspect ratios approaching 0.10.

Recommendations for future work in this area include modeling turbulent behavior; incorporating variable fluid properties with temperature and simulating the

results using a supercomputer; implementing slip boundary conditions for modeling gas flows; modeling surface roughness; incorporating fluid/surface wetting functions into the momentum equations; and solving transient problems.

REFERENCES

[1]   A. Bar-Cohen, Thermal Management of Air- and Liquid-Cooled Multichip Modules, *IEEE Trans.*, *Components, Hybrids, and Manufacturing Technology*, vol. 10, pp. 159-175, 1987.

[2]   D. B. Tuckerman and R. F. W. Pease, High-Performance Heat Sinking for VLSI, *IEEE Electron Device Letters*, vol. EDL-2, pp. 136-139, 1981.

[3]   K. Kawano, K. Minakami, H. Iwasaki, and M. Ishizuka, Development of Micro Channels Heat Exchanging, *Proc. ASME Heat Transfer Division: Application of Heat Transfer in Equipment, Systems, and Education*, Anaheim, California, 1998, vol. 3, pp. 173-180.

[4]   Y. Yener, S. Kakac, M. Avelino, and T. Okutucu, Single-Phase Forced Convection in Microchannels: A State of the Art Review, in: S. Kakac, L. L. Vasiliev, Y. Bayazitoglu, and Y. Yener (Eds.), *Microscale Heat Transfer: Fundamentals and Applications*, Series II, vol. 193, Springer, Dordrecht, Netherlands, pp. 1-24, 2004.

[5]   A. Bontemps, Measurements of Single-Phase Pressure Drop and Heat Transfer Coefficient in Micro and Minichannels, in: S. Kakac, L. L. Vasiliev, Y. Bayazitoglu, and Y. Yener (Eds.), *Microscale Heat Transfer: Fundamentals and Application*s, Series II, vol. 193, Springer, Dordrecht, Netherlands, pp. 25-46, 2004.

[6]   S. V. Patankar, *Numerical Heat Transfer and Fluid Flow*, Hemisphere, New York, 1980.

[7]   I. Papautsky, J. Brazzle, T. Ameel, and A. B. Frazier, Laminar Fluid Behavior in Microchannels Using Micropolar Fluid Theory, *Sensors and Actuators A*, vol. 73, pp. 101-108, 1999.

[8]   P. Wu and W. A. Little, Measurement of Friction Factors for the Flow of Gases in Very Fine Channels Used for Microminiature Joule-Thomson Refrigerators, *Cryogenics*, no. 5, pp. 273-277, 1983.

[9]   J. Pfahler, J. Harley, H. Bau, and J. N. Zemel, Gas and Liquid Flow in Small Channels, *Proc. ASME Micromech. Sensors, Actuators, and Systems*, DSC-vol. 32, pp. 49-60, 1991.

[10]   S. B. Choi, R. F. Barron, and R. O. Warrington, Fluid Flow and Heat Transfer in Microtubes, *Proc. ASME Micromech. Sensors, Actuators, and Systems*, DSC-vol. 32, pp. 123-134, 1991.

[11] D. Yu, R. Warrington, R. Barron, and T. Ameel, An Experimental and Theoretical Investigation of Fluid Flow and Heat Transfer in Microtubes, *Proc. 4th ASME/JSME Thermal Engineering Joint Conf.,* Maui, Hawaii, 1995, vol. 1, pp. 523-530.

[12] P. Wilding, J. Pfahler, H. H. Bau, J. N. Zemel, and L. J. Kricka, Manipulation and Flow of Biological Fluids in Straight Channels Micromachined in Silicon, *Clin. Chem,* vol. 40, pp. 43-47, 1994.

[13] G. M. Mala and D. Li, Flow Characteristics of Water in Microtubes, *Int. J. Heat and Fluid Flow*, vol. 20, pp. 142-148, 1999.

[14] H. Y. Wu and P. Cheng, An Experimental Study of Convective Heat Transfer in Silicon Microchannels with Different Surface Conditions, *Int. J. Heat and Mass Transfer*, vol. 46, pp. 2547-2556, 2003.

[15] H. Ok, H. Park, W. Carr, J. Morris, and J. Zhu, Particle-Laden Drop Impacting on Solid Surfaces, *J. Dispersion Science and Technology*, vol. 25, pp. 449-456, 2004.

[16] B. Agostini, B. Watel, A. Bontemps, and B. Thonon, Liquid Flow Friction Factor and Heat Transfer Coefficient in Small Channels: An Experimental Investigation, *Experimental Thermal and Fluid Science*, vol. 28, pp. 97-103, 2004.

[17] A. Mehta and A. Helmicki, First Principles Based Approach to Modeling of Microfluidic Systems, *Proc. SPIE, Microfluidic Devices and Systems*, Santa Clara, California, 1998, vol. 3515, pp. 205-215.

[18] K. C. Toh, X. Y. Chen, and J. C. Chai, Numerical Computation of Fluid Flow and Heat Transfer in Microchannels, *Int. J. Heat and Mass Transfer*, vol. 45, pp. 5133-5141, 2002.

[19] M. N. Sabry, Scale Effects on Fluid Flow and Heat Transfer in Microchannels, *IEEE Trans., Components and Packaging Technologies*, vol. 23, pp. 562-567, 2000.

[20] B. Xu, K. Ooi, N. T. Wong, and W. K. Choi, Experimental Investigation of Flow Friction for Liquid Flow in Microchannels, *Int. Comm. Heat Mass Transfer*, vol. 27, pp. 1165-1176, 2000.

[21] A. G. Federov and R. Viskanta, Three-Dimensional Conjugate Heat Transfer in the Microchannel Heat Sink for Electronic Packaging, *Int. J. Heat and Mass Transfer*, vol. 43, pp. 399-415, 2000.

[22] B. Xu, K. T. Ooi, C. Mavriplis, and M. E. Zaghloul, Evaluation of Viscous Dissipation Effects for Liquid Flow in Microchannels, *J. Micromechanics and Microengineering*, vol. 13, pp. 53-57, 2003.

[23] C. P. Tso and S. P. Mahulikar, The Use of the Brinkman Number for Single Phase Forced Convective Heat Transfer in Microchannels, *Int. J. Heat Mass Transfer*, vol. 41, pp. 1759-1769, 1998.

[24] J. Koo and C. Kleinstreuer, Liquid Flow in Microchannels: Experimental Observations and Computational Analyses of Microfluidics Effects, *J. Micromechanics and Microengineering,* vol. 13, pp. 568-579, 2003.

[25] F. P. Incropera and D. P. DeWitt, *Fundamentals of Heat and Mass Transfer*, 5th ed., John Wiley & Sons, New York, 2002.

[26] R. K. Shah and A. L. London, *Laminar Flow Forced Convection in Ducts*, Academic Press, New York, 1978.

[27] S. H. Kim, N. K. Anand, and L. S. Fletcher, Free Convection Between Series of Vertical Parallel Plates with Embedded Line Heat Sources, *ASME J. Heat Transfer*, vol. 113, pp. 108-115, 1991.

[28] H. K. Versteeg and W. Malalasekera, *An Introduction to Computational Fluid Dynamics: The Finite Volume Method*, Prentice Hall, London, 1995.

[29] J. G. B. Saldana, Numerical Simulation of Mixed Convection Over a Three-Dimensional Horizontal Backward-Facing Step, Ph.D. dissertation, Texas A&M University, College Station, USA, 2005.

[30] S. C. Chapra and R. P. Canale, *Numerical Methods for Engineers*, 4th ed., McGraw Hill, Boston, 2002.

[31] N. K. Anand, J. G. McMath, and J. M. Choi, Cyclic Tri-Diagonal Matrix Algorithm (CTDMA), Course Handout: *MEEN 644 - Numerical Methods of Heat Transfer and Fluid Flow*, Texas A&M University, College Station, Texas, pp. 1-10, 1994.

[32] N. Kim, N. K. Anand, and D. L. Rhode, A Study on Convergence Criteria for a SIMPLE-Based Finite Volume Algorithm, *Numerical Heat Transfer,* Part B, vol. 34, pp. 401-417, 1998.

[33] W. Qu, and I. Mudawar, Analysis of Three-Dimensional Heat Transfer in Micro-channel Heat Sinks, *Int. J. Heat and Mass Transfer*, vol. 45, pp. 3973-3985, 2002.

VITA

Justin Dale Mlcak was born in Houston, TX, and he was raised in Frydek, TX prior to entering collegiate studies. He received his Bachelor of Science degree in mechanical engineering from Texas A&M University in College Station, TX in May 2004. He received his Master of Science degree in mechanical engineering at Texas A&M University in College Station, TX in May 2007. His subject interests include numerical methods, thermodynamics, heat transfer, dynamics, and controls. Any correspondence should be addressed:

c/o Dr. N.K. Anand

Department of Mechanical Engineering

Texas A&M University

College Station, TX 77843-3123